symmetry

MDPI

Review

B3LYP and B3PW Simulations of ABO_3 Perovskite (001) Surfaces, Interfaces, and Oxygen Vacancies Therein

Roberts I. Eglitis [1,*], Juris Purans [1], Anatoli I. Popov [1], Ran Jia [2] and Sergei P. Kruchinin [3]

[1] Institute of Solid State Physics, University of Latvia, 8 Kengaraga Str., LV1063 Riga, Latvia; juris.purans@cfi.lu.lv (J.P.); popov@latnet.lv (A.I.P.)
[2] Laboratory of Theoretical and Computational Chemistry, Institute of Theoretical Chemistry, Jilin University, Changchun 130023, China; jiaran@jlu.edu.cn
[3] Bogolyubov Institute for Theoretical Physics, NASU, 03143 Kyiv, Ukraine; sergeikruchinin@yahoo.com
* Correspondence: rieglitis@gmail.com; Tel.: +371-26426703

Abstract

The results of most B3LYP and B3PW simulations, performed during the last quarter of century, dealing with ABO perovskite (001) surfaces, heterostructures, and oxygen vacancies therein, were reviewed. According to carried out B3LYP and B3PW simulations, almost all upper-layer atoms on the BO_2- and AO-terminated STO, BTO, PTO, CTO, SZO, BZO, PZO, and CZO perovskite (001) surfaces shift inwards. Practically all ABO perovskite second-layer atoms shift upwards. Finally, nearly all third-layer atoms, once more, shift inwards. The ABO perovskite (001) surface energies, for both BO_2 and AO terminations, are comparable. Computer simulations on the ABO perovskites indicate a significant rise of the B-O chemical bond covalency nearby the BO_2-terminated (001) surfaces in comparison to their bulk. B3LYP- and B3PW-simulated ABO perovskite bulk Γ-Γ band gaps are decreased nearby their BO_2- and AO-terminated (001) surfaces. We discuss recent B3PW simulations for the STO/BTO, STO/PTO, and SZO/PZO (001) heterostructures. Simulated optical band gaps of the STO/BTO, STO/PTO, and SZO/PZO (001) heterostructures mainly depend on the BO_2- or AO-terminations of the upper layer of the augmented film. The displacement magnitudes of the nearest neighbor atoms, around the (001) surface oxygen vacancy, in the ABO perovskites, usually, are larger than in their bulk. In the STO, BTO, PTO, and SZO perovskites, the electronic charge, ordinarily, is a lot better localized inside the bulk than the (001) surface oxygen vacancy. In the STO, BTO, PTO, and SZO perovskites, the (001) surface oxygen vacancy-induced defect levels are located closer to the conduction band bottom than in the bulk cases. Simulated formation energy difference between the bulk and the (001) surface oxygen vacancies in the STO, BTO, PTO, and SZO perovskites triggers the oxygen vacancy segregation from the bulk towards the (001) surface. All computer simulations for ABO perovskites were performed in their high-symmetry cubic phase.

Keywords: ABO_3 perovskites; (001) surfaces; surface energies; B3PW; STO/BTO (001) interface; STO/PTO (001) heterostructure; oxygen vacancy; Γ-Γ band gap

Academic Editor: Sergio Caprara

Received: 6 February 2026
Revised: 16 March 2026
Accepted: 22 March 2026
Published: 24 March 2026

1. Introduction

Surface and interface aspects going on in the ABO_3-type perovskite oxide materials are vitally important questions in present-day solid state physics [1–23]. The entire amount of $SrTiO_3$ (STO), $BaTiO_3$ (BTO), $PbTiO_3$ (PTO), $CaTiO_3$ (CTO), $SrZrO_3$ (SZO), $BaZrO_3$ (BZO), $PbZrO_3$ (PZO), and $CaZrO_3$ (CZO) materials corresponds to the association of ABO_3 perovskite oxides [24–27]. For our purposes, A = Sr, Ba, Pb or Ca, while B = Ti or Zr [28]. ABO_3

perovskites have a lot of technologically important applications [29]. ABO_3 perovskite's technologically important applications involve, for example, photocatalysis, electrocatalysis, fuel cells as well as many others [30]. For instance, STO can provide numerous new opportunities in photocatalytic applications [31]. The BTO-based capacitor is studied as one of the competitors for pulsed power systems because of its high permittivity [32]. The ferroelectric PTO displays extraordinary spontaneous polarization as well as photoelectric qualities, situating it as an encouraging polar photocatalyst [33]. CTO is known to be a significant photocatalyst for splitting water into oxygen and hydrogen [34]. SZO perovskite is of major importance for applications as the high-temperature proton conductor [35]. SZO also displays resistance switching [36,37], ferroelectric ordering [38,39], as well as powerful luminescence [40]. The ABO_3 perovskite, BZO, may be applicable as the refractory material as well as the high-temperature proton conductor [41]. PZO (001) films are encouraging electrical energy storage systems owing to their very significant energy storage density [42]. CZO is a good contender for applications in mechanical filters as well as coatings [43,44]. CZO also possesses numerous electrical implementations, including capacitors and resonators [43,44]. Due to this industrial importance, the ABO_3 perovskite (001) surface terminations have been broadly examined during the last half century [45–84].

As temperature lowers, all eight ABO_3 perovskite oxides exhibit various structural phase transitions [85]. Namely, at room temperature (RT), BZO [86] and STO [87] perovskites have cubic structures [86,87]. At RT, CTO [88], SZO [89], PZO [90], and CZO [91] perovskites possess orthorhombic structures [88–91]. At the same time, PTO at RT exhibits a tetragonal structure [92]. BTO at RT undergoes the tetragonal to orthorhombic phase transition [93].

Generated by the stormy progress of arising technologies, the ABO_3 (001) surfaces were investigated worldwide experimentally during the last half century. For instance, the BTO (001) surface was experimentally explored by photoelectron spectroscopy, as well as LEED (low-energy electron diffraction) and Auger electron spectroscopy [72]. Electronic states and the structure of the BTO (001) surface were examined using scanning tunneling microscopy (STM) and spectroscopy [94]. Barret et al. [59] employed LEEM to investigate the development of the surface shape of BTO (001) in the course of the ferroelectric to paraelectric phase transformation at RT [59]. Berlich et al. [95] examined the BTO (001) surface by different electron spectroscopic methods. MIE and UP spectra supply direct proof of a BaO-terminated BTO (001) surface [95].

On the theory side, the first ab initio computations in the world of BTO (001) surfaces were performed by Padilla et al. in 1997 [96]. They performed ab initio computations of (001) surfaces of BTO in the cubic and tetragonal phases [96]. Using a semi-empirical shell model, Heifets et al. in 1997 [97] computed the surface relaxation of the BTO (001) surface. The first computation in the world for the STO (001) surface was performed by Kimura et al. in 1995 [98] by means of the pseudopotential method. Using the semi-empirical Hartree–Fock (HF) method, Goniakowski et al. [99] in 1996 studied the STO (001) surface. In 1998, Heifets et al. [100] investigated the polarization effect of the STO (001) surface. They computed the relaxation of ions in several upper STO (001) surface layers [100]. Cheng et al. [101] performed ab initio computations for SrO- and TiO_2-terminated STO (001) surface geometry relaxation, and surface energy. Heifets et al. [50] in 2000 employed a semi-empirical shell approach in order to compute the (001) surface relaxation of BTO and STO perovskites. Heifets et al. [45] in 2001 computed the STO (001) surface relaxation as well as rumpling for two terminations (TiO_2 and SrO). Computations were performed employing the ab initio HF method and different DFT-based methods using various exchange-correlation functionals [45]. Erdman et al. [47,102] in 2002 investigated the structure and chemistry of the TiO_2-terminated STO (001) surface. They used a combination of ab initio DFT methods

and experimental HREM microscopy [47,102]. Johnston et al. [103] in 2004 investigated the (1 × 1) and (2 × 1) reconstructions of the STO (001) surface by means of the FP-LMTO method [103]. STO (001) surface energies have been computed [103], and (1 × 1) surfaces were predicted to be energetically stable for different considered conditions [103]. Piskunov et al. [104] in 2005 carried out comparative ab initio computations for AO- and BO_2-terminated STO, BTO, and PTO (001) surfaces' atomic and electronic structure [104]. Wang et al. [105] in 2006 performed first ab initio computations for cubic CTO (001) surfaces with TiO_2 and CaO terminations [105]. Eglitis and Vanderbilt [1] in 2007 carried out ab initio computations for surface relaxations and rumplings of the BTO and PTO perovskite (001) surfaces by means of the hybrid B3PW exchange–correlation functional [1]. In 2007 Eglitis [106] performed ab initio computations for BZO (001) surface atomic relaxation, rumpling, and surface energy for two terminations (ZrO_2 and BaO) employing the B3PW functional [106]. In 2008 Eglitis and Vanderbilt [2,3] carried out ab initio computations for STO and CTO perovskite (001) surface atomic relaxations, rumplings, and surface energies [2,3]. Kotomin et al. [107] in 2008 performed ab initio computations for PZO (001) surfaces with both ZrO_2 and PbO terminations [107]. According to thermodynamical analysis of PZO (001) surfaces [107], the ZrO_2-terminated (001) surface is energetically more stable than the PbO-terminated surface [107]. Wang et al. [108] in 2009 computed the TiO_2 and AO-terminated ATO perovskite (001) surfaces. They computed [108] the surface atomic relaxation and surface grand potential, as well as surface and cleavage energies. Eglitis and Rohlfing [109] in 2010 accomplished ab initio computations for PZO and SZO (001) surface atomic relaxations and rumplings, as well as optical band gaps and charge distribution [109]. Dionot et al. [110] in 2014 employing ab initio computations, explored the BTO (001) surface polarization, domain ordering, and rumpling. Shanavas et al. [111] in 2016, employing ab initio computations, investigated the origin of the Rashba spin-splitting effect [111] in the 2D electron gas on the STO (001) surface. Slassi et al. [112] in 2017 carried out ab initio computations dealing with relaxations of surface atoms, electronic structure, and surface energies of SnO_2- and BaO-terminated BSO (001) surfaces [112]. Saghayezhian et al. [113], in 2019, by means of ab initio calculations, demonstrated that the Ti-O chemical bonds are more covalent near the STO (001) surface than in the STO bulk [113]. Costa-Amaral et al. [48] in 2020 performed ab initio computations dealing with the adsorption of 3D transition metals on the TiO_2- and BaO-terminated BTO perovskite (001) surfaces [48]. Guedes et al. [114] conjoined the ARPES spectroscopy with DFT computations and examined the surface electronic structure of bent STO (001) wafers [114]. Zhou et al. [115] in 2023 performed ab initio computations for BTO (001) surface piezocatalytic properties [115]. Finally, Azevedo et al. [116] in 2024 explored the outcome of Ag doping on the STO (001) surface structure [116].

Schafranek et al. [117] in 2011 investigated the formation of the interface between PTO and STO perovskites by means of in situ photoelectron spectroscopy [117]. Wu et al. [118] in 2012 investigated the STO/BTO interfaces for promising applications for electronic devices [118]. Shah et al. [119] in 2008 performed ab initio computations for the geometrical, ferroelectric, and chemical properties of very complex three-component STO/BTO/PTO perovskite heterostructures [119]. Gao et al. [120] in 2013 performed ab initio computations dealing with the ferroelectric behavior of three-component ultrathin films of CTO/BTO/STO embedded between electrodes [120]. Jiang et al. [121] in 2015 explored 2D electric dipole sheets in the BTO/BZO heterostructure [121]. The authors used first principles-based Monte Carlo computations as well as DFT simulations [121]. Piskunov and Eglitis [76,122], in 2015, by means of B3PW computations, demonstrated that the Gamma–Gamma band gap of the BTO/STO (001) heterostructure mostly depends on TiO_2- or BaO-termination of the upper layer [76,122]. Piskunov et al. [64,123]

in 2016 computed the electronic and atomic structure of PZO/SZO and BTO/STO (001) heterostructures [64,123]. The Gamma–Gamma band gap of PZO/SZO and BTO/STO (001) heterostructures mostly depends on the upper-layer AO or BO2 termination [64,123]. Eglitis et al. [46,124–126] in 2016 computed at an ab initio level the PTO/STO (001) interfaces. Our computed [46,124–126] PTO/STO (001) interface band gaps are in all cases smaller than the respective PTO and STO bulk band gaps. In a study performed by Shoron et al. [127] in 2017, BTO films have been deposited on doped STO channels. The BTO thin films, in spite of their small thickness, are ferroelectric [127]. Cao et al. [128] in 2018, using ab initio DFT computations and experimental STM investigations, reported a room temperature, very complex 2D BTO/STO/LTO heterostructure [128]. Bonini et al. [129] in 2019, using the first principles-based bulk layer approach, predicted the polarization and superlattice structure for PTO/BTO, BTO/STO, and PTO/STO heterostructures [129]. Jia et al. [130] in 2020 investigated the atomic as well as electronic structure of 2D freestanding BTO/STO interfaces [130]. Piyanzina et al. [131] in 2021 performed ab initio computations dealing with the atomic as well as electronic structure of the BTO/STO heterostructure and explored the influence of ferroelectric polarization on it. Chen et al. [132] in 2022 explored asymmetric LMO/BTO/STO heterostructures constructed onto a silicon platform [132]. Yang et al. [133], in 2023, by means of the phase field approach, demonstrated that the vortex structure arises in the BTO/STO heterostructure [133]. Finally, in 2024, Gómez-Ortiz et al. [134] performed MD (molecular dynamics) computations of PTO/STO heterostructures to explore the extraordinary properties of this transformation [134].

Eglitis et al. [135] in 1997 carried out combined ab initio LMTO and semi-empirical INDO (intermediate neglect of differential overlap) computations of oxygen vacancy with two trapped electrons in KNO perovskite [135]. Park et al. [136] in 1998 computed the relaxation of atoms surrounding the oxygen vacancy in PTO perovskite [136]. A blue photoluminescence band in STO was measured at RT by Zhang et al. [137] in 1999. It was detected [137] that the oxygen vacancies in STO are responsible for this experimentally measured visible emission band. Donnerberg et al. [138] in 2000 carried out ab initio HF and DFT computations for neutral oxygen vacancies in BTO perovskite. According to their results, the isolated oxygen vacancies create deep electronic levels in the band gap of BTO perovskite [138]. Astala et al. [139] in 2001 carried out ab initio computations for oxygen vacancies in the STO matrix. The authors [139] performed the atomic relaxation around the oxygen vacancy defect in STO. They also computed the relevant electron densities and Mulliken atomic charges [139]. Stashans et al. [140] in 2002 studied the F-centers and oxygen vacancies on the polar STO (011) surface. Using the semi-empirical INDO theoretical studies, the relaxation of atoms around the F-centers and oxygen vacancies was computed [140]. Muller et al. [141] in 2004 outline the oxygen vacancy concentrations in STO on an atomic scale, making use of STEM and XPS. The absolute detection sensitivity of one to four oxygen vacancies in the STO matrix was demonstrated [141]. Carrasco et al. [142] in 2006 computed the relaxation of atoms as well as the electronic structure around the F-center in the STO matrix. The formation energy and the energy barriers for F-center defect migration in STO were computed [142]. Lee et al. [143] in 2007 computed the oxygen vacancy formation energy in BTO perovskite and found it to be larger than in the STO matrix [143]. Alexandrov et al. [144] in 2009, by means of the B3PW functional, computed the atomic and electronic characteristics of oxygen vacancies in the STO bulk and on its (001) surfaces. The oxygen vacancies in STO perovskite induce more shallow defect energy levels in the band gap of its (001) surfaces than in the STO bulk [144]. Choi et al. [145] in 2011 computed the atomic as well as electronic structure of oxygen vacancy in BTO perovskite by means of a hybrid HF and DFT exchange–correlation functional. El-Mellouhi et al. [146] in 2013 performed ab initio computations of oxygen vacancies in

STO. The oxygen vacancies induced in the STO perovskite create a microscopic tetragonal elongation of the lattice in the z direction [146]. According to Chen et al. [147], oxygen vacancies in BTO crystal may improve its electrocatalytic activity [147]. Clabel et al. [148] in 2017 demonstrated that the luminescence spectra in BTO may be explained via the recombination of the self-trapped excitons. They induced localized states inside the BTO-forbidden band gaps, created by oxygen vacancies and impurities [148]. According to Al-Zubi et al. [149], the conductive properties of the STO crystal are considerably affected by the presence of oxygen vacancies. Rusevich et al. [150] in 2021 computed the atomic as well as electronic structure of oxygen vacancies in STO perovskite by means of ab initio calculations. The ab initio computed oxygen vacancies in the STO perovskite are mostly located on their (001) surfaces [150]. Yang et al. [151] in 2023 demonstrated that in STO perovskite, oxygen vacancies play a significant function in photoactivation processes [151]. Finally, Wang et al. [152] in 2025 examined how the layer of oxygen vacancies affects the BTO perovskite atomic structure and its electronic properties.

The goal of this review paper was to summarize the quarter-of-a-century-long study dealing with ABO perovskites. The work reported here deals mostly with B3LYP and B3PW simulations of ABO perovskite (001) surfaces, heterostructures, and oxygen vacancies. As a starting point, we compiled results dealing with AO- and BO_2-terminated ABO perovskite (001) surfaces. The next part of paper is devoted to STO/BTO, STO/PTO and SZO/PZO (001) heterostructures. The final part of the review deals with B3LYP and B3PW simulations of oxygen vacancies in ABO perovskite bulk and on their (001) surfaces.

2. Computational Methods

2.1. ABO Perovskite (001) Surface Structure and Energies

The B3LYP and B3PW simulations for eight ABO perovskite (001) surfaces were implemented making use of the CRYSTAL software system [153]. Mainly, the hybrid exchange–correlation functionals B3LYP [154] and B3PW were used [155,156]. Additional simulations were carried out using the complementary ab initio Hartree–Fock (HF) approach [157]. Moreover, ab initio computations for ABO perovskite bulk Γ-Γ band gaps were in addition executed using the Generalized Gradient approximation [158] developed by Perdew and Wang (GGA-PW) [155,156]. It is noteworthy to mention that the HF method [157] considerably overestimates the experimental band gaps of different complex materials [1–3,159,160]. At the same time, DFT-based methods [161,162], for example, GGA-PW [155,156], significantly underestimate the band gaps of complex materials [1–3,159,160]. It is self-evident that B3LYP or B3PW hybrid exchange–correlation functionals, which make use of 20% of the HF approach and 80% of the DFT Hamiltonian, allow to obtain admirable results for the band gaps of complex materials. Primarily for this reason, the B3LYP and B3PW functionals were utilized in most of ensuing simulations. The pivotal role of the CRYSTAL software package is its utilization of the 2D isolated slab pattern [153]. The reciprocal space integration was executed using the $8 \times 8 \times 8$ times expanded Pack–Monkhorst [163] mesh for ABO perovskite bulk and $8 \times 8 \times 1$ times extended k-point net for their (001) surfaces.

For BO_2-terminated ABO perovskite (001) surface (Figure 1) B3LYP and B3PW simulations, the symmetrical slabs [1–3,64,79,106] were utilized. They are made up of 9 mixing BO_2 and AO layers perpendicular to the z-axis [1–3,64,79]. The 9-layer slab, employed in ABO (001) surface simulations, from the top and bottom, ended with BO_2 planes (Figure 1). It consisted of a supercell holding 23 atoms (Figure 1). The slab was non-stoichiometric with unit cell formula $A_4B_5O_{14}$ [1–3,45]. The second 9-layer ABO perovskite (001) slab was demarcated from both sides with AO layers (Figure 2). It consisted of 9 alternating AO and BO_2 layers (Figure 2) and housed 22 atoms. This slab was non-stoichiometric with the unit cell formula $A_5B_4O_{13}$ (Figure 2). The classical Mulliken population investigation for both

the chemical bonding and covalency effects in the ABO perovskite bulk and on their (001) surfaces [78,164,165] was utilized.

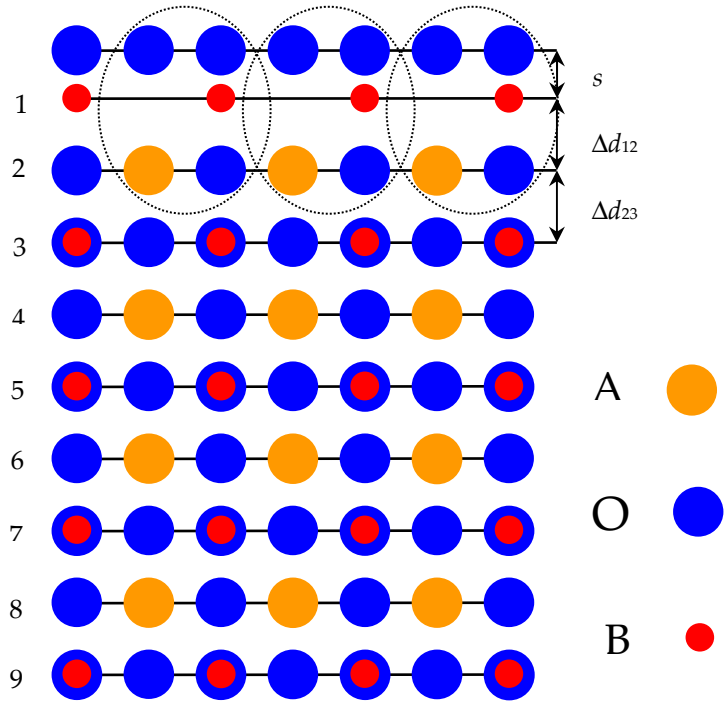

Figure 1. Outline of the 9-layer BO_2-terminated ABO perovskite (001) surface [79].

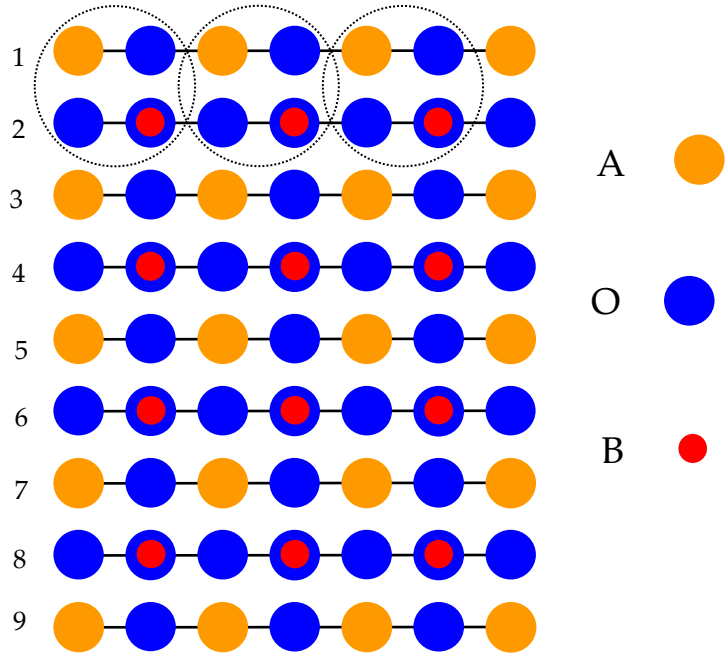

Figure 2. Outline of the 9-layer AO-terminated ABO perovskite (001) surface [79].

To begin with ABO perovskite (001) surface energy simulations, the AO- and BO_2-terminated (001) surface cleavage energy [1–3,45,76] were computed. In performed ABO perovskite cleavage energy simulations, the 9-layer AO- and BO_2-terminated (001) slabs housed 22 and 23 atoms, respectively [1–3,45,79]. Thereby, these two slabs together represented 9 ABO perovskite bulk unit cells, which in summary housed 45 atoms [1–3,64,79,106]:

$$E_{surf}{}^{unr}(AO + BO_2) = ¼ [E_{slab}{}^{unr}(AO) + E_{slab}{}^{unr}(BO_2) - 9E_{bulk}], \quad (1)$$

where (AO + BO_2) means that the ABO perovskite cleavage energy is equal for both AO and BO_2 terminations [1–3,45,79]. $E_{slab}{}^{unr}$(AO) and $E_{slab}{}^{unr}$(BO_2) are the unrelaxed AO- or BO_2-terminated 9-layer-containing ABO perovskite (001) slab's total energies. E_{bulk} is the ABO perovskite 5-atom-containing unit cell's total energy [1–3,76,77].

$$E_{rel}(\lambda) = ½ [E_{slab}{}^{rel}(\lambda) - E_{slab}{}^{unr}(\lambda)], \quad (2)$$

where λ denotes AO or BO_2. $E_{slab}{}^{rel}$(λ) and $E_{slab}{}^{unr}$(λ) are the 9-layer slab's total energies after and without the structure relaxation, respectively [1–3,76,77]. The ABO perovskite (001) surface energy may be simulated using the following formula:

$$E_{surf}(\lambda) = E_{surf}{}^{unr}(AO + BO_2) + E_{rel}(\lambda). \quad (3)$$

2.2. B3LYP- and B3PW-Simulation Details for the STO/BTO, STO/PTO, and SZO/PZO (001) Interfaces

To our next point, we will discuss the simulation details and atomic structure of BTO/STO (001) heterostructure (Figure 3) [122–126]. Simulation details and the atomic structure of related STO/PTO and SZO/PZO (001) interfaces are almost identical [122–126].

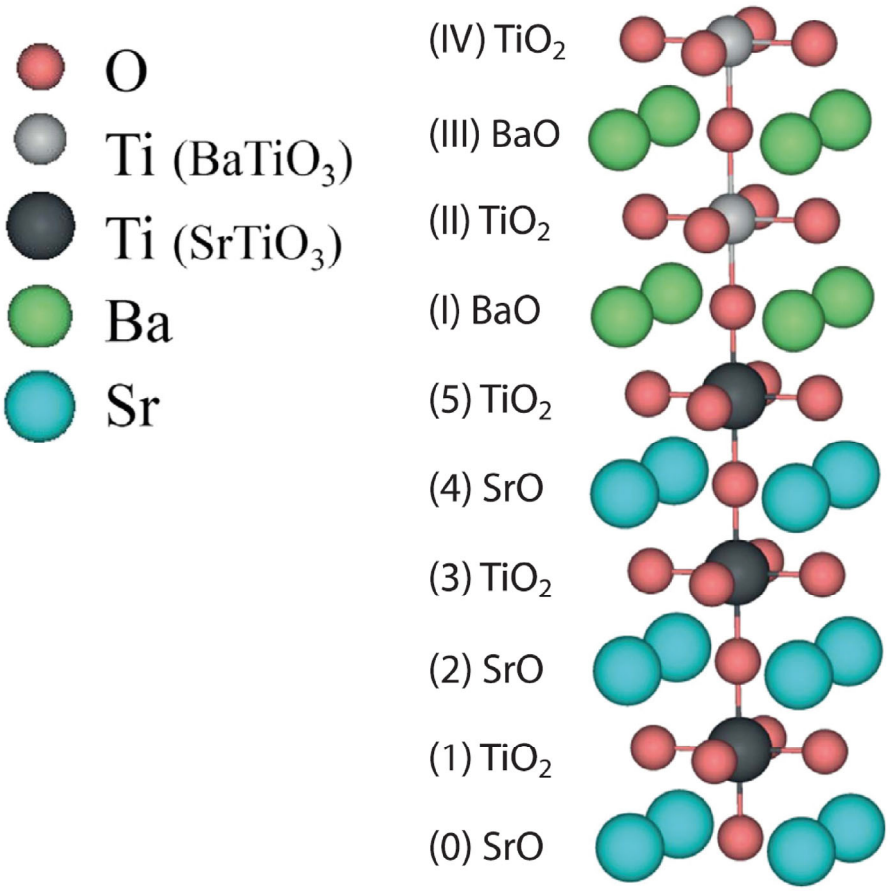

Figure 3. Sketch of the (001) interface between BTO and STO perovskites [125,126].

Both BTO and STO perovskites were simulated employing their high-symmetry $Pm\bar{3}m$ cubic structure (Figure 3) [1–3,64,79]. In B3PW simulations, the STO perovskite (001) substrate consists of 11 periodic SrO and TiO_2 monolayers (Figure 3) [122–126]. Between 1 and 10 periodic BaO and TiO_2 monolayers were augmented on both sides of the 11-layer STO (001) substrate (Figure 3). Thereby, B3PW-simulated BTO/STO (001) heterostructure consisted of 31 monolayers (Figure 3). Originating from symmetry restrictions, the atomic

shifts in the BTO/STO (001) interface are allowed only alongside the *z*-axis (Figure 3). In B3PW computations of displacement Δz, the shift of the previous monolayer (Figure 3) was taken into account. The reference coordinate *z* for each monolayer *N* was simulated using the following equation:

$$z_N{}^{\mathrm{ref}} = ½ \left[z_{N-1}{}^{Me} + z_{N-1}{}^{O}\right) \quad (4)$$

In Equation (4) $z_{N-1}{}^{Me}$ and $z_{N-1}{}^{O}$ describe the *z* coordinates for a cation and an anion located in the previous monolayer.

2.3. B3LYP- and B3PW-Simulation Details for the Bulk and (001) Surface F-Centers in SZO

In B3PW simulations using CRYSTAL code, all 3 SZO perovskite atoms ought to have localized basis sets (BSs). Namely, for Sr and O atoms, the BSs from Ref. [166] were used. For the Zr atom the BS from the CRYSTAL software home page [153] was used. The bulk *F*-center B3PW simulations in the SZO matrix were carried out using a 3 × 3 × 3 times expanded supercell (Figure 4). Consequently, the B3PW simulations for a system containing 134 SZO bulk atoms as well as the single *F*-center (Figure 4) were performed.

For the *F*-center simulations located on the ZrO_2-terminated SZO (001) surface, a 2D 11-layer-containing slab model [1–3,167] was utilized. A modified conjugate gradient algorithm [168,169] to find an energy minimum for the potential energy surface around the (001) surface *F* center was employed. The *F*-center situated on the ZrO_2-terminated SZO (001) surface employing a 3 × 3 × 1 times expanded surface supercell (Figure 5) [170] was simulated. With the goal to compute the surface *F*-center, the one of the O atoms located on the ZrO_2-terminated SZO (001) surface (Figure 5) [170] were removed. In this way, in the B3PW simulations the surface *F*-center concentration on the ZrO_2-terminated SZO (001) surface is equal to 1/18, or 5.56% (Figure 5) [170].

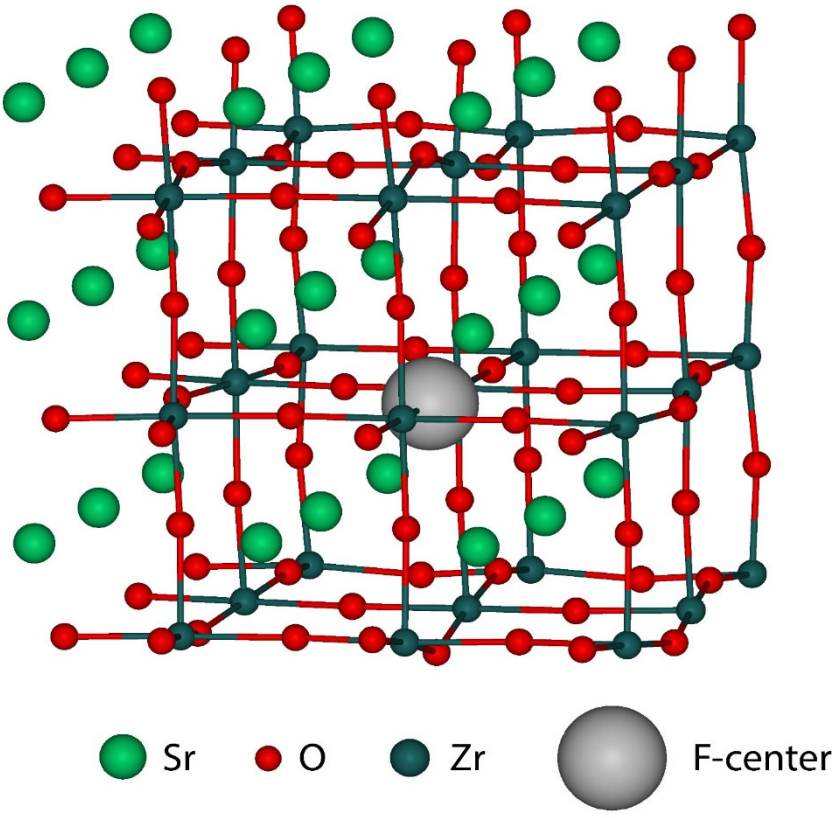

Figure 4. Sketch of the 3 × 3 × 3 times extended SZO bulk supercell containing a single *F*-center [170].

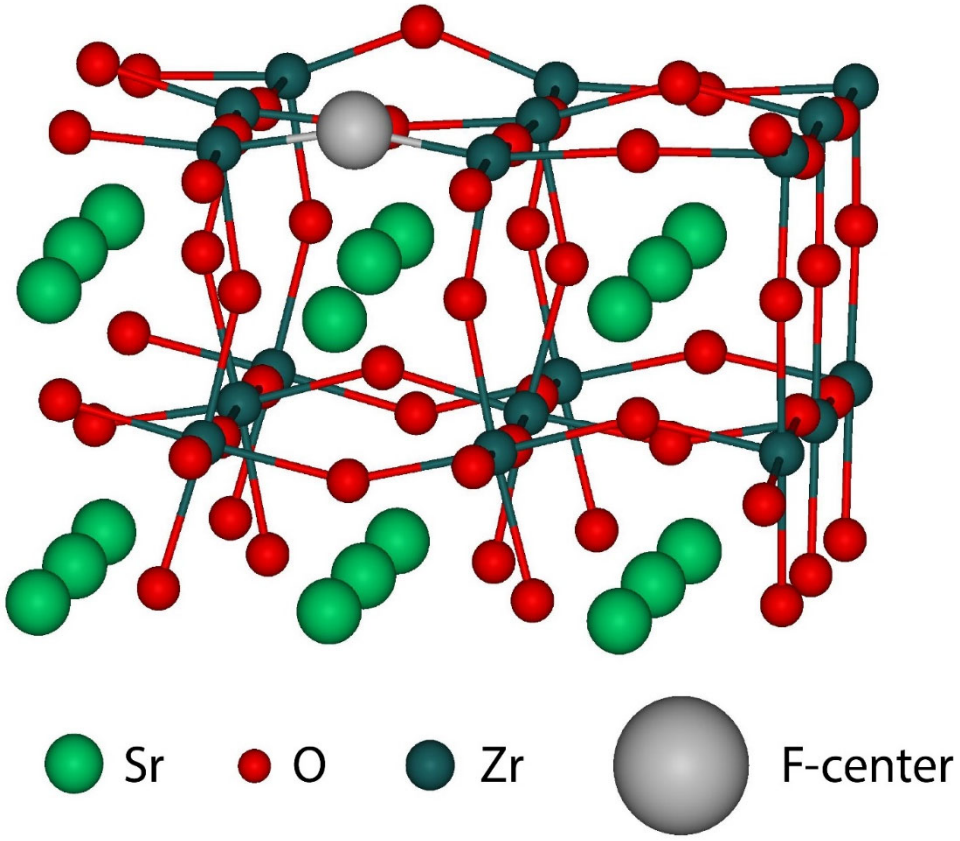

Figure 5. Sketch of the ZrO_2-terminated SZO (001) surface holding the surface *F*-center [170].

3. B3LYP- and B3PW-Simulation Results for ABO Perovskite Bulk and Their (001) Surfaces

3.1. B3LYP- and B3PW-Simulation Results for ABO Perovskite Bulk

To begin with, during last quarter of century, using B3LYP and B3PW hybrid exchange–correlation functionals, the eight ABO perovskite bulk lattice constants (Table 1) [1–3,57,79,106,109,166,171] were simulated. B3LYP and B3PW simulated ABO perovskite bulk lattice constants [1–3,57,79,106,109,166,171] were compared with obtainable experimental data (Table 1) [172–177]. From Table 1 it follows that in most cases the B3LYP-simulated ABO perovskite bulk lattice constants are larger than the B3PW-simulated ones (Table 1) [1–3,57,79,106,109,166,171].

Table 1. B3LYP-, B3PW-, HF-, and GGA-PW-simulated ABO perovskite bulk lattice constants (in Å) [1–3,57,79,106,109,166,171]. Experimental measurement data [172–177] are listed for comparison.

ABO Perovskite	Method	Theory	Experiment
STO	B3LYP	3.94 [166]	3.89 [172]
	B3PW	3.904 [2]	
BTO	B3LYP	4.04 [166]	4.00 [172]
	B3PW	4.008 [1]	
PTO	B3LYP	3.96 [166]	3.97 [173]
	B3PW	3.936 [1]	

Table 1. *Cont.*

ABO Perovskite	Method	Theory	Experiment
CTO	B3LYP	3.851 [57]	3.8967 [174]
	B3PW	3.851 [3]	
	GGA-PW	3.884 [79]	
	HF	3.863 [79]	
SZO	B3LYP	4.195 [109]	4.154 [175]
	B3PW	4.155 [79]	
	GGA-PW	4.176 [79]	
	HF	4.182 [79]	
BZO	B3LYP	4.234 [109]	4.199 [176]
	B3PW	4.234 [106]	
	GGA-PW	4.240 [79]	
	HF	4.250 [79]	
PZO	B3LYP	4.220 [109]	4.1614 [177]
CZO	B3LYP	4.157 [171]	-

Namely, B3LYP-simulated ABO perovskite bulk lattice constants are larger than B3PW-simulated ones for STO, BTO, PTO, and SZO perovskites [1–3,57,79,106,109,166,171], whereas for CTO and BZO perovskites, B3LYP- and B3PW-simulated bulk lattice constants coincide (Table 1). All B3LYP- and B3PW-simulated ABO perovskite bulk lattice constants are in a fair agreement with available experimental data [172–177] (Table 1). For instance, the B3PW-simulated BTO bulk lattice constant of 4.008 Å [1,46,79,166], only by 0.008 Å, or 0.2% of lattice constant a_0, exceeds the experimental value of 4.00 Å [172]. Furthermore, B3PW-simulated SZO bulk lattice constant of 4.155 Å [79] is even in a better agreement with the experimental value of 4.154 Å [175]. B3LYP-simulated CZO perovskite bulk lattice constant of 4.157 Å [171] in fact is a theoretical prediction. There are no available experimental data for the CZO bulk lattice constant in the cubic phase (Table 1). The largest disagreement between the B3LYP-simulated [109] and experimentally measured bulk lattice constant is for PZO perovskite. Specifically, the B3LYP-simulated PZO perovskite bulk lattice constant (4.220Å) [109], by 0.0586Å, or 1.41%, exceeds the experimental value of 4.1614Å [177].

For instance, B3PW-simulated effective atomic charges in the STO bulk are equal to (+1.871*e*) on the Sr atom, (+2.351*e*) on the Ti atom and (−1.407*e*) on the O atom (Table 2) [2]. B3PW-simulated effective atomic charges in the BTO bulk are equal to (+1.797*e*) on the Ba atom, (+2.367*e*) on the Ti atom, and (−1.388*e*) on the O atom (Table 2) [1]. The smallest simulated A atom effective charge is on the PTO perovskite Pb atom (+1.354*e*), whereas the largest one is on the SZO perovskite Sr atom (+1.880*e*) (Table 2). In contrast, the smallest simulated B atom effective charge is on the PZO perovskite Pb atom (2.111*e*), whereas the largest one is on the BTO perovskite Ba atom (2.367*e*) (Table 2) [1,109]. The smallest chemical bond population value between B and O atoms B-O is in the CTO perovskite bulk (0.084*e*) (Table 2) [3]. Just opposite, the largest B-O chemical bond population value is in the BZO perovskite bulk (0.108*e*) (Table 2) [106]. It is interesting to note that the B3PW-simulated B-O chemical bond population values for the BTO (+0.098*e*) and PTO (+0.098*e*) perovskite bulk coincide (Table 2) [1,79] (Table 2).

Table 2. B3PW- and B3LYP-simulated ABO perovskite bulk atomic charges $Q(e)$ and bond populations $P(e)$ [1–3,76,77,106,109,171].

Perovskite		**STO**	**BTO**	**PTO**	**CTO**	**SZO**	**BZO**	**PZO**	**CZO**
Ion	**Property**	**B3PW**	**B3PW**	**B3PW**	**B3PW**	**B3LYP**	**B3PW**	**B3LYP**	**B3LYP**
A	Q	+1.871	+1.797	+1.354	+1.782	+1.880	+1.815	+1.368	+1.787
	P	−0.010	−0.034	+0.016	+0.006	+0.002	−0.012	+0.030	+0.014
O	Q	−1.407	−1.388	−1.232	−1.371	−1.351	−1.316	−1.160	−1.310
	P	+0.088	+0.098	+0.098	+0.084	+0.092	+0.108	+0.106	+0.086
B	Q	+2.351	+2.367	+2.341	+2.330	+2.174	+2.134	+2.111	+2.144

STO B3PW- (3.96 eV) [166] and B3LYP-simulated (3.89 eV) [166] bulk Γ-Γ band gaps are in a fair consensus with the experimental data (3.75 eV) [178] (Table 3). At the same time, the HF-simulated [166] STO Γ-Γ band gap (12.33 eV) strongly, more than three times, overestimates the experimental value of (3.75 eV) [178] (Table 3). On the other hand, the GGA-PW-simulated STO bulk Γ-Γ band gap (2.31 eV) [166] underestimates the experimental bulk Γ-Γ band gap value of (3.75 eV) [178] (Table 3). B3PW- (3.55 eV) [166] as well as B3LYP-simulated (3.49 eV) [166] BTO bulk Γ-Γ band gaps are almost two times larger than the GGA-PW-simulated (1.97 eV) BTO bulk Γ-Γ band gap (Table 3) [166]. The HF-simulated BTO bulk Γ-Γ band gap (11.73 eV) is more than three times larger than the B3PW- and B3LYP-simulated band gap values [166] (Table 3). The B3PW-simulated BTO bulk Γ-Γ band gap is depicted in Figure 6 [104] (Table 3).

Table 3. B3PW-, B3LYP-, GGA-PW- and HF-simulated ABO perovskite bulk Γ-Γ band gaps (in eV) [79,109,166,179]. Experimental results are mentioned for comparison [178,180].

Simulated Material	**Functional**	**Theory, Γ-Γ Band Gap**	**Experiment**
STO	B3PW	3.96 [166]	3.75 [178]
	B3LYP	3.89 [166]	
	GGA-PW	2.31 [166]	
	HF	12.33 [166]	
BTO	B3PW	3.55 [166]	-
	B3LYP	3.49 [166]	
	GGA-PW	1.97 [166]	
	HF	11.73 [166]	
PTO	B3PW	4.32 [166]	-
	B3LYP	4.15 [166]	
	GGA-PW	2.61 [166]	
	HF	12.74 [166]	
CTO	B3PW	4.18 [79]	-
	B3LYP	4.20 [79]	
	GGA-PW	2.34 [79]	
	HF	12.63 [79]	

Table 3. *Cont.*

Simulated Material	Functional	Theory, Γ-Γ Band Gap	Experiment
SZO	B3PW	5.30 [109]	-
	B3LYP	5.31 [109]	
	GGA-PW	3.53 [109]	
	HF	13.54 [109]	
BZO	B3PW	4.93 [79]	5.3 [180]
	B3LYP	4.79 [179]	
	GGA-PW	3.24 [79]	
	HF	12.96 [79]	
PZO	B3LYP	5.63 [109]	-
	GGA-PW	3.86 [109]	
	HF	13.89 [109]	

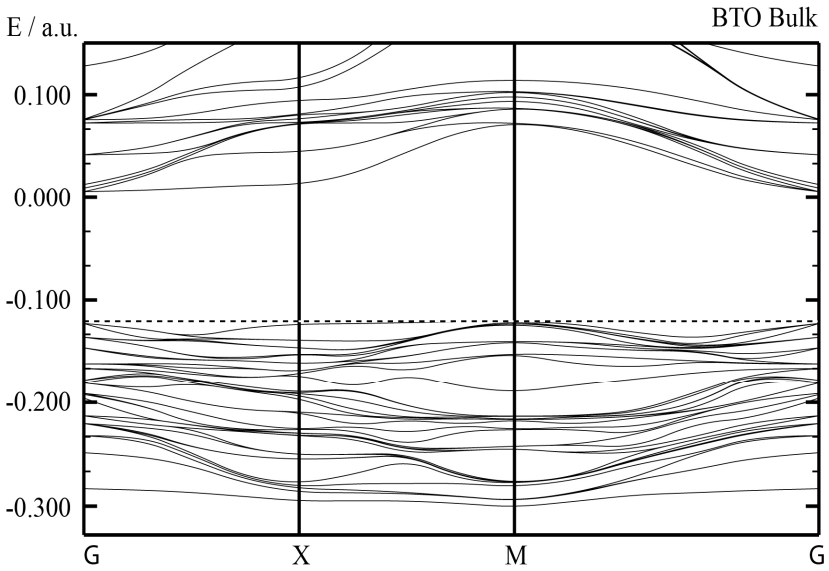

Figure 6. B3PW-simulated BTO perovskite bulk electronic band structure [104,125].

B3PW- (4.32 eV) [166] and B3LYP-simulated (4.15 eV) [166] PTO bulk Γ-Γ band gaps are appreciably larger than the GGA-PW-simulated (2.61 eV) ones (Table 3) [166]. The HF-simulated PTO bulk Γ-Γ band gap (12.74 eV) [166] is roughly three times larger than the respective B3PW- (4.32 eV) and B3LYP-simulated (4.15 eV) bulk band gaps (Table 3) [166]. The B3PW-simulated PTO bulk Γ-Γ band gap as well as the electronic band structure are depicted in Figure 7 (Table 3) [166].

In the end, B3PW-simulated (4.93 eV) [79] as well as B3LYP-simulated (4.79 eV) [179] BZO bulk band gap Γ-Γ values are in fine agreement with the experiment (5.3 eV) (Table 3) [180]. The GGA-PW-simulated (3.24 eV) [79] BZO bulk Γ-Γ band gap, by 2.06 eV, appreciably underestimates the experimental BZO bulk Γ-Γ band gap value of 5.3 eV [180]. The HF-simulated (12.96 eV) [79] BZO bulk Γ-Γ band gap significantly, by 2.45 times, overestimated the experimental BZO bulk Γ-Γ band gap value of 5.3 eV [180]. The B3PW-simulated BZO perovskite bulk electronic band structure is illustrated in Figure 8 [79] (Table 3).

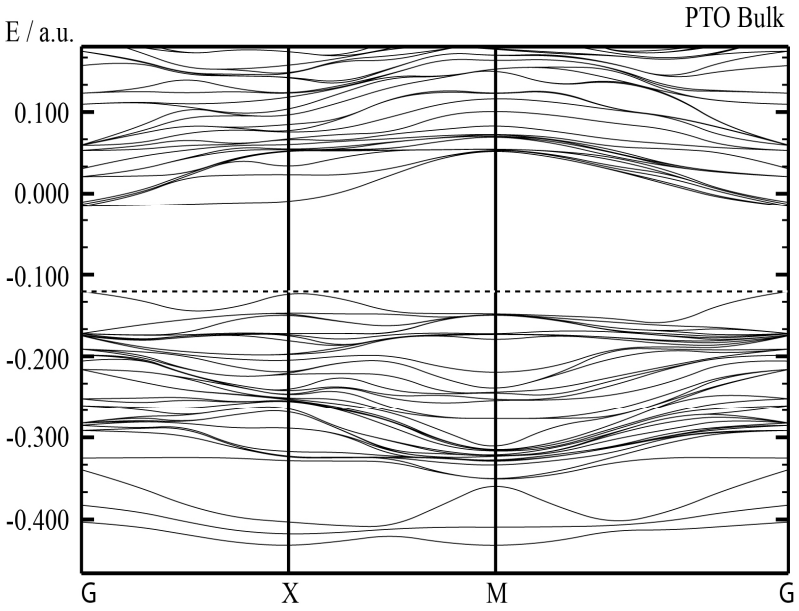

Figure 7. B3PW-simulated PTO perovskite bulk electronic band structure [104,125].

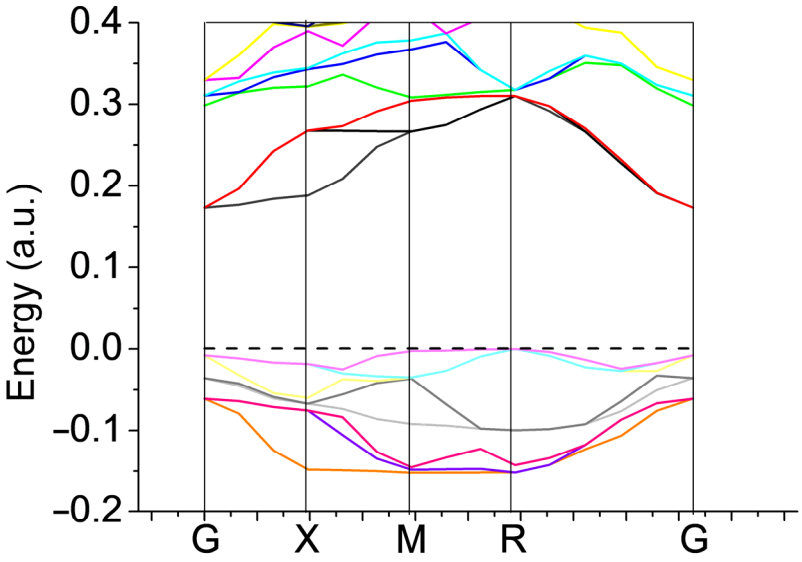

Figure 8. B3PW-simulated BZO perovskite bulk electronic band structure [79].

GGA-PW- (1), B3LYP- (3) and HF-computed (4) STO, BTO, PTO, CTO, SZO, BZO and PZO perovskite Γ-Γ band gaps are depicted in Figure 9. The available experimental data for STO (3.75 eV) [178] and BZO (5.3 eV) [180] perovskite cubic phases (2) are listed for comparison purposes (Figure 9). As we can see from Table 3 and Figure 9, the B3LYP exchange–correlation functional allows to achieve the best agreement with the experiment for the ABO perovskite bulk Γ-Γ band gaps. At the same time, the HF approach overestimates the experimental STO and BZO bulk Γ-Γ band gap by roughly three times (Table 3 and Figure 9). On the other hand, the GGA-PW exchange–correlation functional, by roughly 1.6 times, underestimate the STO and BZO bulk Γ-Γ band gap (Table 3 and Figure 9). It is worth noting that a similar trend is valid also for other materials, for example CaF_2 [159,160]. The experimentally measured CaF_2 Γ-Γ band gap is equal to 12.1 eV [159,160]. The CaF_2 Γ-Γ band gap is greatly underestimated when using the LDA to the DFT functional (8.72 eV) [159,160]. From another perspective, similar to the ABO perovskites, the HF-simulated CaF_2 Γ-Γ band gap is almost two times overestimated (20.77 eV) [159,160].

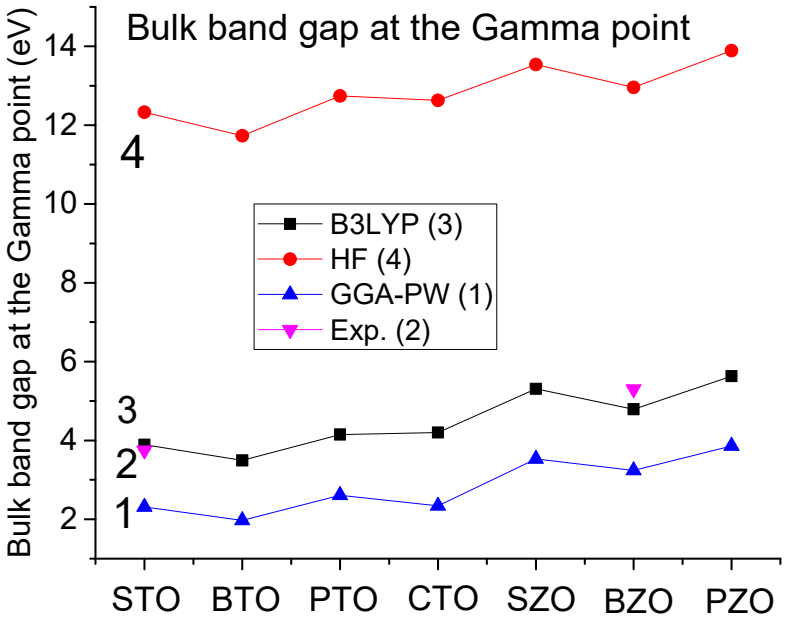

Figure 9. GGA-PW- (1), B3LYP- (3) and HF-computed (4) bulk band gaps at the Gamma point for seven ABO perovskites. Available experimental data (2) for STO and BZO perovskites are plotted for comparison purposes.

3.2. B3LYP and B3PW Simulations of ABO Perovskite (001) Surfaces

The B3PW- and B3LYP-simulated relaxation of the ABO perovskite BO_2- and AO-terminated (001) surface upper-two- or three-layer atoms are listed in Table 4 [1–3,106,109,171].

Table 4. B3LYP- and B3PW-simulated BO_2- and AO-terminated ABO perovskite (001) surface atomic relaxations (% of a_0).

Perovskite		**STO**	**BTO**	**PTO**	**CTO**	**SZO**	**BZO**	**PZO**	**CZO**
Termination		**TiO_2**	**TiO_2**	**TiO_2**	**TiO_2**	**ZrO_2**	**ZrO_2**	**ZrO_2**	**ZrO_2**
Layer	**Ion**	**B3PW**	**B3PW**	**B3PW**	**B3PW**	**B3LYP**	**B3PW**	**B3LYP**	**B3LYP**
1	B	−2.25	−3.08	−2.81	−1.71	−1.38	−1.79	−2.37	−1.30
	O	−0.13	−0.35	+0.31	−0.10	−2.10	−1.70	−1.99	−2.31
2	A	+3.55	+2.51	+5.32	+2.75	+2.81	+1.94	+4.36	+4.23
	O	+0.57	+0.38	+1.28	+1.05	+0.91	+0.85	+1.04	+1.25
3	B	-	-	-	-	−0.04	−0.03	−0.47	−0.05
	O	-	-	-	-	−0.05	0.00	−0.28	−0.09
Termination		**SrO**	**BaO**	**PbO**	**CaO**	**SrO**	**BaO**	**PbO**	**CaO**
Layer	**Ion**	**B3PW**	**B3PW**	**B3PW**	**B3PW**	**B3LYP**	**B3PW**	**B3LYP**	**B3LYP**
1	A	−4.84	−1.99	−3.82	−8.31	−7.63	−4.30	−5.69	−10.01
	O	+0.84	−0.63	−0.31	−0.42	−0.86	−1.23	−2.37	−0.79
2	B	+1.75	+1.74	+3.07	+1.12	+0.86	+0.47	+0.57	+1.11
	O	+0.77	+1.40	+2.30	+0.01	−0.05	+0.18	+0.09	+0.01
3	A	-	-	-	-	−1.53	−0.01	−0.47	−2.60
	O	-	-	-	-	−0.45	−0.14	−0.47	−0.48

The relaxation of BO_2- and AO-terminated ABO perovskite (001) surface upper two-layer metal atoms, as a rule, is larger than the same layer oxygen atoms (Table 4). There are only

two exceptions to this systematic trend (Table 4). Namely, the ZrO_2-terminated SZO and CZO (001) surface upper-layer Sr and Ca atom displacements are smaller than the respective oxygen atom displacements (Table 4). Another systematic trend for BO_2- and AO-terminated ABO perovskite (001) surfaces is inwards relaxation of most of the upper-layer atoms (Table 4). At one time, most of the second-layer atoms relax upwards, while most of the third-layer atoms, once more, relax inwards (Table 4). There are only three exceptions to this systematic trend (Table 4). The strongest shift in magnitude between all B3LYP- or B3PW-simulated atoms shows the upper-layer Ca atom on the CaO-terminated CZO (001) surface (Table 4). This B3LYP-simulated CaO-terminated CZO perovskite (001) surface upper-layer Ca atom inward relaxation magnitude is really huge (−10.01% of a_0) [171] in comparison to all other ABO perovskite-simulated atom relaxation magnitudes [1–3,106,109,171] (Table 4).

B3LYP- and B3PW-simulated ABO perovskite (001), (011) and (111) surface energies are collected in Table 5 and Figure 10. All B3LYP- and B3PW-simulated ABO perovskite (001) surface energies are roughly around 1 eV [1–3,106,109,171]. B3LYP- and B3PW-simulated AO- and BO_2-terminated ABO perovskite (001) surface energies are comparable (Table 5 and Figure 10). The largest energy difference (0.46 eV) is between the CaO-terminated CZO (001) surface (0.87 eV) and ZrO_2-terminated CZO (001) surface (1.33 eV). At the same time, B3PW-simulated BZO perovskite BaO (1.30 eV) and ZrO_2-terminated (1.31 eV) (001) surface energies almost coincide (Table 5 and Figure 10). The largest B3LYP-simulated ABO perovskite (001) surface energy is for the ZrO_2-terminated CZO (001) surface (1.33 eV). By contrast, the smallest B3PW-simulated ABO perovskite (001) surface energy is for the TiO_2-terminated PTO perovskite (0.74 eV). It is noteworthy to mention that earlier simulations performed by Heifets et al. [50], using a very simple mechanical shell model (SM), also yield the similar results [1–3,106,109,171] (Table 5). That is to say that SM-simulated SrO- and TiO_2-terminated STO (001) surface energies are 1.32 eV and 1.36 eV, respectively [50]. Only slightly larger are the SM-simulated BaO and TiO_2-terminated BTO (001) surface energies (1.45 eV and 1.40 eV, respectively) [50]. For both STO and BTO perovskites, these SM-simulated (001) surface energies are comparable and slightly larger than 1 eV [1–3,50,106,109,171] (Table 5).

Table 5. B3LYP- and B3PW-computed ABO perovskite (001), (011), and (111) surface energies (in eV per surface cell).

Perovskite	**STO**	**BTO**	**PTO**	**CTO**	**SZO**	**BZO**	**PZO**	**CZO**
Termination	Surface energies, (001)							
AO	1.15	1.19	0.83	0.94	1.13	1.30	1.00	0.87
BO_2	1.23	1.07	0.74	1.13	1.24	1.31	0.93	1.33
Termination	Surface energies, (011)							
A	2.66	3.24	2.03	1.91	2.21	2.90	1.74	1.49
BO	3.06	2.04	1.36	3.13	3.61	3.09	1.89	3.46
O	2.04	1.72	1.72	1.86	2.23	2.32	1.85	2.08
Termination	Surface energies, (111)							
B	4.99	7.28	6.14	4.18	7.98	7.94	6.93	8.19
AO_3	6.30	8.40	8.11	5.86	9.45	9.33	8.21	9.62

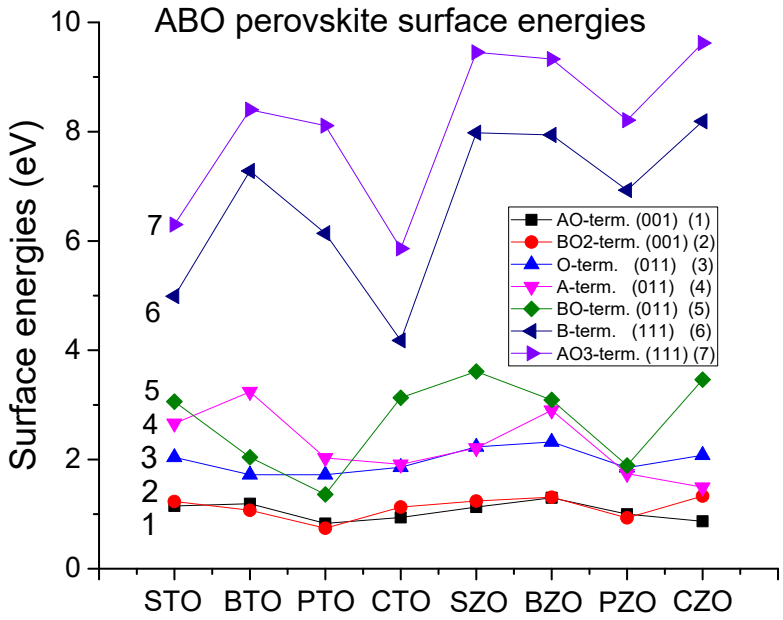

Figure 10. B3LYP- and B3PW-simulated ABO perovskite surface energies; for neutral AO- (line 1) and BO_2-terminated (line 2) ABO (001) surfaces; for polar O-terminated (line 3), A-terminated (line 4), and BO-terminated (line 5) ABO perovskite (011) surfaces; as well as for polar B-terminated (line 6), and AO_3-terminated (line 7) ABO perovskite (111) surfaces (in eV per surface cell).

In contrast, in most cases, there are large energy differences between different terminations (A, BO, O) of ABO perovskite polar (011) surfaces (Table 5 and Figure 10) [1–3,106,109,171]. Namely, the largest ABO perovskite (011) surface energy difference (1.97 eV) is between the A- (1.49 eV) and BO-terminated (3.46 eV) CZO (011) surfaces (Table 5 and Figure 10). On the contrary, for the PZO perovskite, the polar (011) surface energies for all three terminations A (1.74 eV), BO (1.89 eV), and O (1.85 eV) almost coincide (Table 5 and Figure 10) [1–3,106,109,171]. It is worth noting that for all ABO perovskites, their polar (011) surface energies are always larger than the neutral (001) surface energies (Table 5 and Figure 10). Nevertheless, the ABO perovskite polar (111) surface energies are always larger than even their polar (011) surface energies [1–3,106,109,171]. The absolutely largest B3LYP-computed ABO perovskite surface energy (9.62 eV) is for the AO_3-terminated polar CZO (111) surface.

B3LYP- and B3PW-simulation results dealing with ABO perovskite bulk as well as AO- and BO_2-terminated (001) surface Γ-Γ band gaps are collected in Table 6. As we can see from Table 6, the B3PW-simulated STO bulk Γ-Γ band gap (3.96 eV) [104] is in a fair agreement with the available experimental data (3.75 eV) [178]. The STO perovskite AO-terminated (3.72 eV) and BO_2-terminated (3.95 eV) (001) surface Γ-Γ band gaps are reduced regarding the respective STO bulk band gap value (3.96 eV) [104,178] (Table 6).

The B3PW-simulated BTO bulk band gap at Γ-point is equal to 3.55 eV (Table 6) [104,125]. The B3PW-simulated BaO-terminated BTO (001) surface Γ-Γ band gap is equal to 3.49 eV (Figure 11a) [104,125]. The TiO_2-terminated BTO (001) surface electronic band structure is depicted in Figure 11b (Table 6) [104,125]. Its band gap at Γ-point is equal to 2.96 eV (Table 6) (Figure 11b) [104].

The B3PW-simulated PTO bulk Γ-Γ band is equal to 4.32 eV (Table 6) [104]. The B3PW-simulated PbO-terminated PTO (001) surface Γ-Γ band gap is equal to 3.58 eV (Figure 12a), whereas the TiO_2-terminated PTO (001) surface band gap is equal to 3.18 eV (Figure 12b) (Table 6) [104,125]. B3PW-simulated PbO- and TiO_2-terminated PTO (001) surface electronic band structures are depicted in Figure 12a and Figure 12b, respectively [104,125].

Table 6. B3LYP- and B3PW-simulated ABO perovskite bulk and (001) surface Γ-Γ band gaps (in eV). Available experimental data are listed for comparison purposes.

Perovskite	Method	Γ-Γ Band Gap			
		Bulk	AO-t. (001)	BO_2-t. (001)	Experiment
STO	B3PW	3.96 [104]	3.72 [104]	3.95 [104]	3.75 [178]
BTO	B3PW	3.55 [104]	3.49 [104]	2.96 [104]	-
PTO	B3PW	4.32 [104]	3.58 [104]	3.18 [104]	-
CTO	B3PW	4.18 [79]	3.87 [79]	3.30 [79]	-
SZO	B3LYP	5.31 [109]	5.04	4.91	-
BZO	B3PW	4.93 [79]	4.82	4.48	5.3 [180]
PZO	B3LYP	5.63 [109]	3.86	4.60	-
CZO	B3LYP	5.40 [79]	5.00	5.22	-

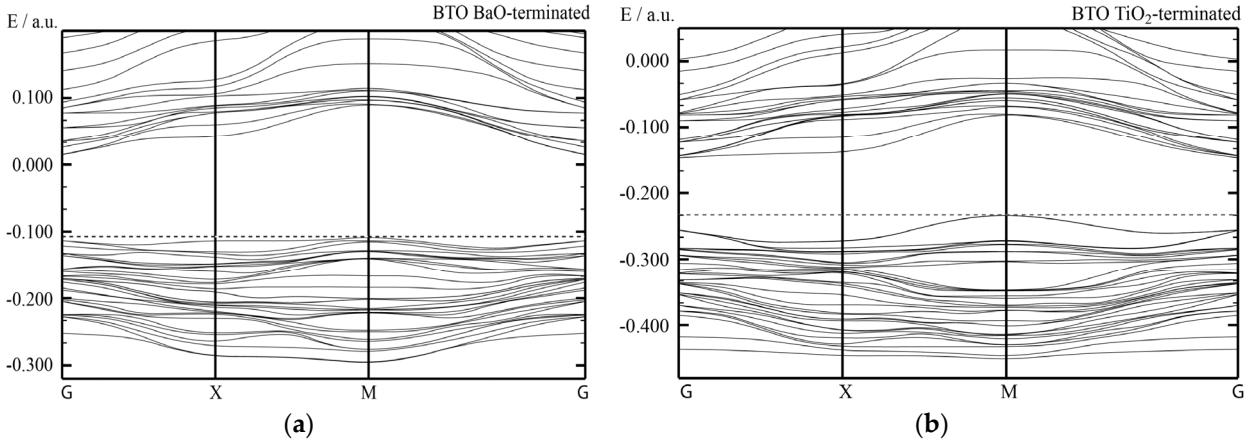

Figure 11. B3PW-simulated BaO- (**a**) and TiO_2-terminated (**b**) BTO perovskite (001) surface electronic band structure [104,125].

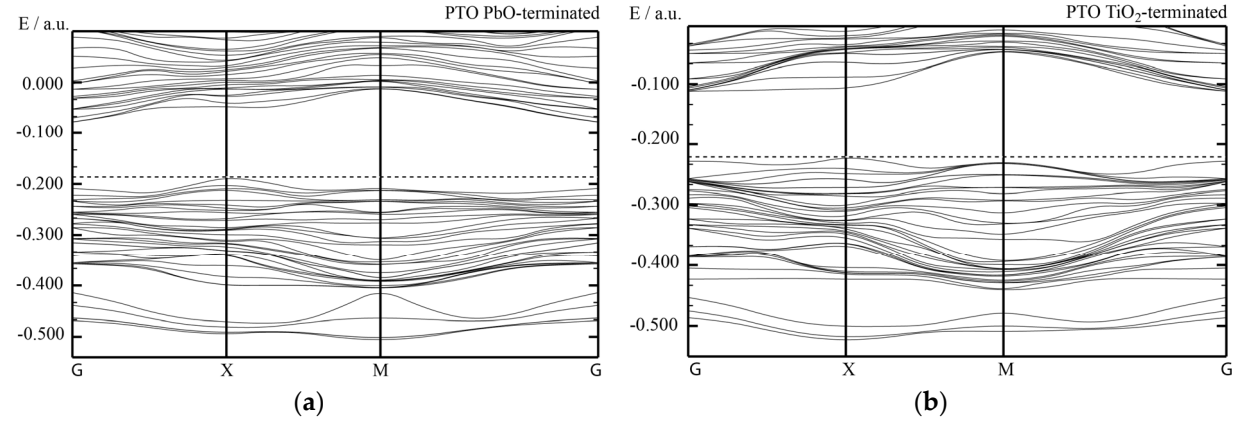

Figure 12. B3PW-simulated PbO- (**a**) and TiO_2-terminated (**b**) PTO perovskite (001) surface electronic band structure [104,125].

The B3PW-simulated BZO bulk band gap at Γ-point is equal to 4.93 eV [79] and is in fair agreement with the available experimental data of 5.3 eV [180] (Table 6). The B3PW-simulated BaO-terminated BZO (001) surface Γ-Γ band gap (Figure 13a) is equal to 4.82 eV, whereas the ZrO_2-terminated BZO (001) surface Γ-Γ band gap is equal to 4.48 eV

(Figure 13b) (Table 6). B3PW-simulated BaO- and ZrO_2-terminated BZO (001) surface electronic band structures are illustrated in Figure 13a and Figure 13b, respectively [79].

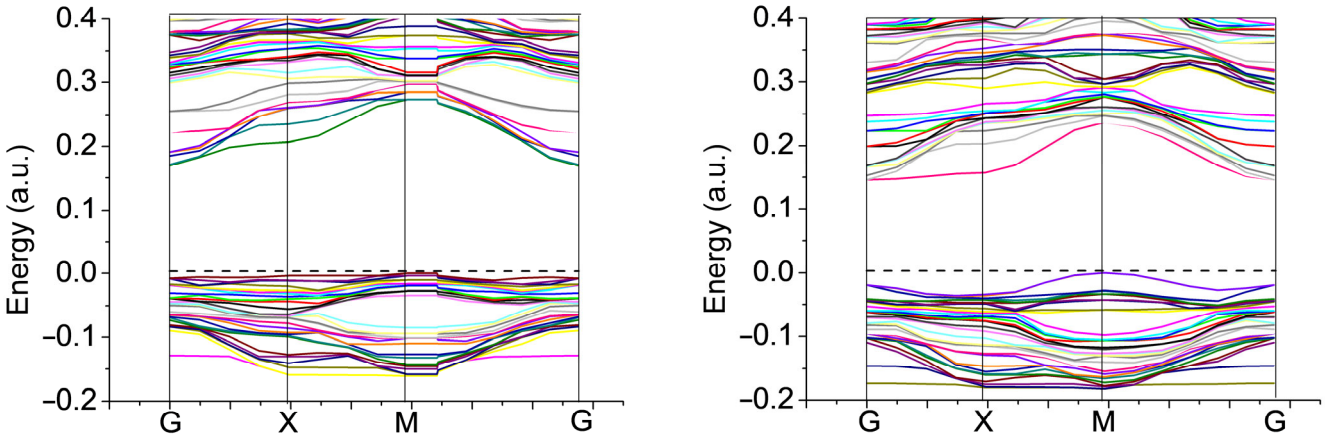

Figure 13. B3PW-simulated BaO- (**a**) and TiO_2-terminated (**b**) BZO perovskite (001) surface electronic band structure [79].

As it is possible to see from Figure 14 and Table 6, B3LYP- and B3PW-simulated ABO perovskite bulk Γ-Γ band gaps always are larger than their (001) surface band gaps. The smallest energy difference is for the STO perovskite bulk (3.96 V) and its BO_2-terminated (001) surface (3.95 eV) Γ-Γ band gaps, only 0.01 eV (Figure 14 and Table 6). Also, for BTO perovskite, the bulk Γ-Γ band gap (3.55 eV) exceeds the AO-terminated BTO (001) surface Γ-Γ band gap (3.49 eV) only by 0.06 eV (Table 6 and Figure 14). For all other B3LYP- or B3PW-simulated ABO perovskites, their bulk Γ-Γ band gaps exceed their (001) surface Γ-Γ band gaps more strongly (Table 6 and Figure 14) [1–3,106,109,171].

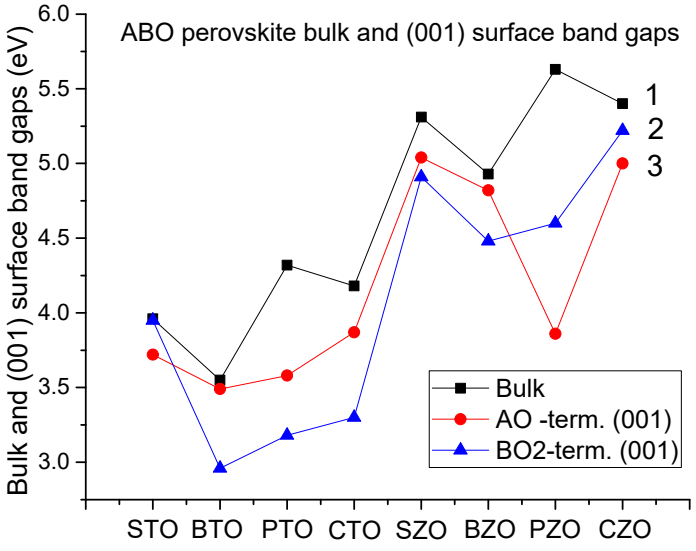

Figure 14. B3PW- and B3LYP-simulated ABO perovskite bulk (1) as well as BO_2- (2) and AO-terminated (3) (001) surface Γ-Γ band gaps (in eV).

As it is possible to see from Table 7 and Figure 15, the B-O atom chemical bond population in the ABO perovskite bulk is always smaller than in its BO_2-terminated (001) surface as well as on the BO-terminated polar (011) surface [1–3,57,79,106,109,166,171]. B3LYP- and B3PW-simulated ABO perovskite bulk B-O chemical bond populations are in

the range from 0.084*e* for the CTO perovskite to 0.108*e* for the BZO perovskite (Table 7 and Figure 15). B3LYP- and B3PW-simulated BO_2-terminated ABO perovskite (001) surface B-O chemical bond populations are in the range from 0.102*e* for the CZO perovskite to 0.132*e* for the BZO perovskite (Table 7 and Figure 15). Finally, the largest B3LYP- and B3PW-simulated B-O atom chemical bond populations are for the polar BO-terminated ABO perovskite (011) surfaces. They are in the range of 0.128*e* for the TiO-terminated CTO perovskite (011) surface to 0.152*e* for the ZrO-terminated BZO perovskite polar (011) surface (Table 7 and Figure 15).

Table 7. B3LYP- and B3PW-simulated ABO perovskite B-O chemical bond populations for their bulk, BO_2-terminated (001) surfaces as well as polar BO-terminated (011) surfaces (in *e*) [1–3,57,79,106,109,166,171].

B-O Chemical Bond Populations in ABO Perovskites								
Perovskite	**STO**	**BTO**	**PTO**	**CTO**	**SZO**	**BZO**	**PZO**	**CZO**
Functional	B3PW	B3PW	B3PW	B3PW	B3LYP	B3PW	B3LYP	B3LYP
Bulk	0.088	0.098	0.098	0.084	0.092	0.108	0.106	0.086
B-O, (001) surf.	0.118	0.126	0.114	0.114	0.114	0.132	0.116	0.102
B-O, (011) surf.	0.130	0.130	0.132	0.128	0.142	0.152	0.148	0.138

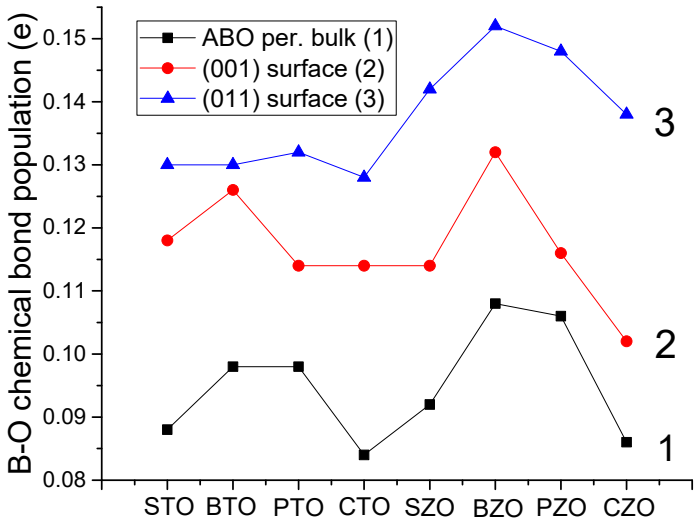

Figure 15. B3LYP- and B3PW-simulated B-O chemical bond populations for ABO perovskite bulk (1) as well as their (001) (2) and (011) (3) surfaces (in *e*) [1–3,57,79,106,109,166,171].

3.3. B3PW-Simulated STO/BTO (001) Heterostructures

By means of B3PW hybrid exchange–correlation functionals, the STO/BTO (001) interfaces were simulated [122,124,125]. In B3PW simulations, the symmetrically terminated slab model [122,124,125] was employed (Figure 3). The STO (001) substrate (Figure 3), used in B3PW simulations, contained 11 atomic layers, and was terminated from both sides by the TiO_2-containing layers [122,124,125]. In the following stage, the layer-by-layer epitaxial growth of the STO/BTO (001) interface (Table 8 and Figure 3) was simulated [122,124,125]. Specifically, the pair of the BTO perovskite (001) layers were always attached on both sides of the 11-layer symmetrical STO substrate (Figure 3) [122,124,125].

Table 8. B3PW-simulated STO/BTO (001) interface atomic charges Q_{atom} (in e), in plane clean charges Q_{plane} (in e), relative in plane displacement Δz (% of a_0) with reference to the perfect bulk locations of the metal atoms and respective band gaps δ (in eV) [122,124,125]. Planes of STO (001) substrate are itemized making use of the Arabic numbers (Figure 3). On the other hand, Roman numbers are employed to itemize the planes of our augmented BTO film. The number 0 describes the central plane of the (001) heterostructure (Figure 3).

Layer	Prop.	STO	BTO1	BTO2	BTO3	BTO4	BTO5	BTO6	BTO7	BTO8	BTO9	BTO10
X	Q_{Ti}											2.30
	Q_O											−1.27
	Q_{plane}											−0.23
	Δz											−3.92
IX	Q_{Ba}										1.75	1.76
	Q_O										−1.48	−1.37
	Q_{plane}										0.27	0.39
	Δz										−2.32	4.60
VIII	Q_{Ti}									2.30	2.37	2.36
	Q_O									−1.26	−1.41	−1.36
	Q_{plane}									−0.23	−0.44	−0.36
	Δz									−3.84	3.65	0.65
VII	Q_{Ba}								1.75	1.76	1.80	1.79
	Q_O								−1.48	−1.37	−1.42	−1.40
	Q_{plane}								0.26	0.39	0.38	0.39
	Δz								−2.21	4.62	0.68	2.12
VI	Q_{Ti}							2.30	2.37	2.36	2.36	2.36
	Q_O							−1.26	−1.40	−1.36	−1.38	−1.37
	Q_{plane}							−0.23	−0.43	−0.36	−0.40	−0.38
	Δz							−3.70	3.69	0.74	1.88	1.50
V	Q_{Ba}						1.75	1.76	1.80	1.79	1.79	1.79
	Q_O						−1.49	−1.38	−1.42	−1.40	−1.41	−1.41
	Q_{plane}						0.26	0.38	0.37	0.39	0.39	0.39
	Δz						−2.07	4.68	0.76	2.15	1.40	1.71
IV	Q_{Ti}					2.30	2.37	2.36	2.36	2.36	2.36	2.36
	Q_O					−1.26	−1.40	−1.36	−1.38	−1.37	−1.38	−1.37
	Q_{plane}					−0.22	−0.43	−0.36	−0.40	−0.38	−0.39	−0.39
	Δz					−3.55	3.73	0.83	1.92	1.57	1.57	1.63
III	Q_{Ba}				1.75	1.76	1.80	1.79	1.79	1.79	1.79	1.79
	Q_O				−1.49	−1.39	−1.43	−1.41	−1.41	−1.41	−1.40	−1.41
	Q_{plane}				0.25	0.38	0.37	0.38	0.39	0.38	0.39	0.38
	Δz				−1.84	4.77	0.89	2.27	1.48	1.79	1.53	1.68
II	Q_{Ti}			2.29	2.37	2.35	2.36	2.36	2.36	2.36	2.36	2.36
	Q_O			−1.25	−1.40	−1.35	−1.38	−1.37	−1.38	−1.37	−1.38	−1.37
	Q_{plane}			−0.21	−0.42	−0.35	−0.39	−0.37	−0.39	−0.38	−0.39	−0.39
	Δz			−3.20	3.83	1.03	2.04	1.72	1.69	1.75	1.60	1.71
I	Q_{Ba}		1.75	1.76	1.80	1.79	1.79	1.79	1.79	1.79	1.79	1.79
	Q_O		−1.51	−1.40	−1.44	−1.43	−1.42	−1.42	−1.42	−1.42	−1.41	−1.42
	Q_{plane}		0.23	0.36	0.35	0.36	0.37	0.37	0.38	0.37	0.38	0.37
	Δz		−1.54	4.87	1.02	2.35	1.53	1.84	1.55	1.70	1.51	1.64

Table 8. *Cont.*

Layer	Prop.	STO	BTO1	BTO2	BTO3	BTO4	BTO5	BTO6	BTO7	BTO8	BTO9	BTO10
5	Q_{Ti}	2.29	2.37	2.35	2.36	2.36	2.36	2.36	2.36	2.36	2.36	2.36
	Q_O	−1.29	−1.41	−1.38	−1.40	−1.39	−1.40	−1.40	−1.40	−1.40	−1.40	−1.40
	Q_{plane}	−0.30	−0.45	−0.40	−0.44	−0.42	−0.44	−0.43	−0.44	−0.44	−0.45	−0.44
	Δz	−5.95	1.96	−1.13	−0.11	−0.46	−0.47	−0.43	−0.56	−0.48	−0.61	−0.53
4	Q_{Sr}	1.85	1.88	1.87	1.87	1.87	1.87	1.87	1.87	1.87	1.87	1.87
	Q_O	−1.37	−1.41	−1.39	−1.38	−1.38	−1.37	−1.38	−1.37	−1.37	−1.36	−1.37
	Q_{plane}	0.48	0.47	0.48	0.50	0.49	0.50	0.50	0.51	0.50	0.51	0.50
	Δz	4.13	−1.32	0.60	−0.43	−0.10	−0.39	−0.26	−0.43	−0.33	−0.47	−0.37
3	Q_{Ti}	2.35	2.36	2.36	2.36	2.36	2.36	2.36	2.36	2.36	2.36	2.36
	Q_O	−1.38	−1.42	−1.41	−1.42	−1.41	−1.42	−1.42	−1.43	−1.42	−1.43	−1.42
	Q_{plane}	−0.42	−0.48	−0.45	−0.48	−0.47	−0.49	−0.48	−0.49	−0.48	−0.49	−0.49
	Δz	−0.96	0.27	−0.20	−0.25	−0.21	−0.38	−0.29	−0.44	−0.35	−0.48	−0.40
2	Q_{Sr}	1.87	1.87	1.87	1.87	1.87	1.87	1.87	1.87	1.87	1.87	1.87
	Q_O	−1.42	−1.40	−1.41	−1.39	−1.40	−1.39	−1.39	−1.38	−1.39	−1.38	−1.39
	Q_{plane}	0.45	0.47	0.46	0.48	0.47	0.49	0.48	0.49	0.48	0.49	0.49
	Δz	0.88	−0.35	0.12	−0.29	−0.15	−0.37	−0.26	−0.42	−0.32	−0.45	−0.37
1	Q_{Ti}	2.35	2.36	2.36	2.36	2.36	2.36	2.36	2.36	2.36	2.36	2.36
	Q_O	−1.40	−1.42	−1.41	−1.42	−1.42	−1.42	−1.42	−1.43	−1.42	−1.43	−1.42
	Q_{plane}	−0.44	−0.47	−0.46	−0.48	−0.47	−0.49	−0.48	−0.49	−0.48	−0.49	−0.49
	Δz	0.14	−0.09	−0.01	−0.27	−0.17	−0.36	−0.26	−0.42	−0.33	−0.46	−0.37
0	Q_{Sr}	1.87	1.87	1.87	1.87	1.87	1.87	1.87	1.87	1.87	1.87	1.87
	Q_O	−1.42	−1.40	−1.41	−1.39	−1.40	−1.39	−1.39	−1.38	−1.39	−1.38	−1.39
	Q_{plane}	0.45	0.47	0.46	0.48	0.47	0.49	0.48	0.49	0.48	0.49	0.49
	Δz	0.00	0.00	0.00	0.00	0.00	0.00	0.00	0.00	0.00	0.00	0.00
	δ	2.58	3.47	2.33	3.29	2.16	3.25	2.10	3.24	2.06	3.22	2.06

To perform B3PW simulations of STO/BTO (001) heterostructures, between one and 10 BTO (001) layers on both sides of the STO substrate were augmented (Table 8 and Figure 3) [122,124,125]. Consequently, 10 STO/BTO (001) heterostructures were constructed (Table 8 and Figure 3). In B3PW simulations, due to symmetry constraints, the relaxation of atoms was carried out only alongside the *z*-axis (Table 8). Were performed B3PW simulations for the atomic shifts (Δz) with respect to the averaged position (z) of the precursory atomic layer, as defined in the Equation (4).

As we see from Table 8 and Figure 16, B3PW-simulated TiO_2-terminated 11-layer-containing STO (001) substrate's upper layer (x = 0 in Figure 16) rather strongly relaxes towards the STO perovskite bulk by (−5.95% of a_0). B3PW simulation results (Table 8) show that the upper BTO (001) layer atoms, which are augmented on the TiO_2-terminated STO substrate, always (Δz) relax inwards (x = 1–10 in Figure 16) [122,124,125]. The BTO perovskite augmented on the STO (001) substrate upper (001) layer atom inward displacement numeric value (Table 8) Δz strongly rests on the even or odd number of upper layers (Figure 16). This characterizes the upper-augmented BTO perovskite (001) layer termination (TiO_2 or BaO) (Table 8 and Figure 16). For instance, in the case of one augmented BTO perovskite (001) layer (x = 1), consisting of both Ba as well as O atoms (Table 8 and Figure 16), the atoms' displacement (Δz) magnitude equals (−1.54% of a_0) [122,124,125]. When two BTO (001) layers are attached, and the top layer contains O and Ti atoms, the respective displacement size Δz equals (−3.20% of a_0) (Table 8 and Figure 16). In the case of three attached BTO (001) layers, the top layer O and Ba atom displacement size Δz equals

(−1.84% of a_0) (Table 8 and Figure 16). When four BTO (001) layers are attached, the top layer O and Ti atom displacement size Δz equals (−3.55% of a_0) (Table 8 and Figure 16).

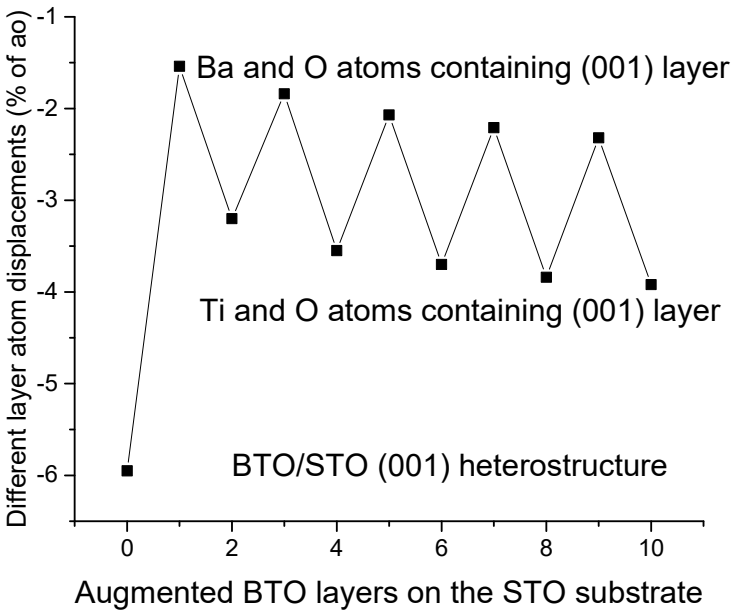

Figure 16. B3PW-simulated top-layer atom displacement sizes Δz (% of a_0) for 11-layer STO perovskite substrate (x = 0) and for 10 augmented BTO (001) layers (x = 1–10) [122,124,125].

In Table 8 are collected B3PW-simulated total Mulliken charges for the STO and BTO perovskite (001) atomic planes TiO_2, SrO and BaO [122,124,125]. At the B3PW level, they were simulated, as well as the specific atomic charges for all separate atoms located on the planes Q_{Ti}, Q_{Sr}, Q_{Ba} and Q_O (Table 8). B3PW-simulated Mulliken atomic charges of atoms in the BTO and STO perovskite bulk are collected in Table 2 [122,124,125]. According to performed B3PW simulations, the Ti-O chemical bond covalency near the TiO_2-terminated STO (0.118*e*) and BTO (0.126*e*) (001) surfaces increases with respect to its respective bulk values 0.088*e* for STO and 0.100*e* for BTO (Table 2) [122,124,125]. We want to stress that, according to performed B3PW simulations [122,124,125], related effects are observed also around the STO/BTO (001) interfaces. Namely, the increase in the Ti-O atom chemical bond covalency from the BTO perovskite bulk (0.100*e*) tp (0.126*e*) near the STO/BTO (001) interface [122,124,125]. Results of performed B3PW simulations [122,124,125] show that the upper-layer planes of the TiO_2-terminated BTO (001) 10-layer thin films, placed on the 11-layer STO (001) substrate attract additional 0.23*e* (Table 8) [122,124,125]. It is worth noting, that B3PW-simulated BaO-terminated STO/BTO (001) heterostructures (Figure 3) become more positively charged, in order to recompensate for the surface relaxation (Table 8) [122,124,125].

B3PW-simulated difference electron charge density maps for the STO/BTO (001) interfaces are illustrated in Figure 17. B3PW-simulated difference electron charge density maps (Figure 17) exhibit that the key distortion happens at the (001) heterostructure (Figure 17). It is caused by the restructuring of the surface effects of the (001) slabs (Figure 17) [122,124,125].

Figures 18 and 19 illustrate B3PW-simulated DOS, expressed layer by layer for all atomic orbitals of the Ba, Sr, Ti as well as O atoms for the three- and four-UC-thick STO/BTO (001) interfaces (Figures 18 and 19). The B3PW-simulated top of the valence band (VB) consists mostly of the O 2*p* orbitals. The B3PW-simulated bottom of the conduction band (CB) consists mostly of the Ti 3*d* states (Figures 18 and 19). It is worth noting that the hybridization between the Ti as well as O atoms is very strong (Figures 18 and 19).

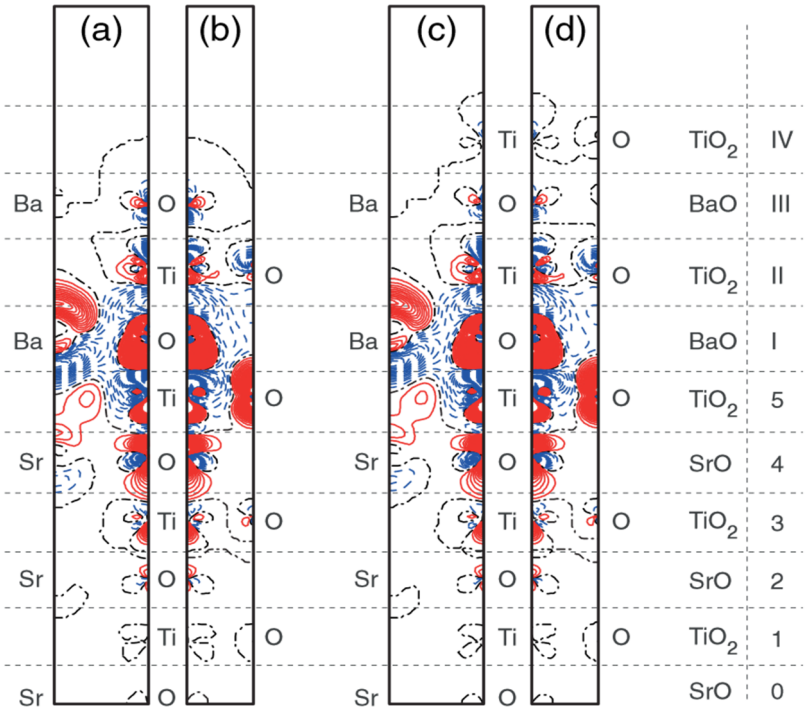

Figure 17. B3PW-simulated difference electron charge density graphs for STO/BTO (001) heterostructures. (**a**) (110) cross-section for N_{BTO} = 3. (**b**) (100) cross-section for N_{BTO} = 3. (**c**) (110) cross-section for N_{BTO} = 4. (**d**) (100) cross-section for N_{BTO} = 4. Blue dashed, red solid as well as black dash–dot isolines define negative, positive as well as no difference in charge density. Isodensity curves are designed from −0.025 to +0.025*e* Å^{-3} employing the increment of 0.0005*e* Å^{-3}. Right-hand bar shows from which layer the atoms were originated. STO and BTO layers were numbered starting from the center of slab [125].

The B3PW-simulated STO perovskite direct bulk band gap (3.96 eV) (Table 3) [166] is in fair agreement with the available experimental data of 3.75 eV [178]. Also, the B3PW-simulated BTO perovskite direct bulk band gap of 3.55 eV (Table 3) [166] is in good agreement with the available experimental measurements performed at 278 K temperature. For the B3PW-simulated BaO-terminated STO/BTO (001) interface (Figure 18), the computed surplus of the electron density enlarges the occupied levels, giving rise to the enlarged band gap (Table 8 and Figure 20). On the contrary, according to performed B3PW simulations, the TiO_2-terminated STO/BTO (001) interface (Figure 19) encounters the deficiency of the electron density, which reduces the occupied levels. Thereby, the band gaps of the stoichiometric STO/BTO (001) interfaces are lowered (Figure 20).

3.4. B3PW-Simulated STO/PTO (001) Heterostructures

As an STO/PTO (001) heterostructure substrate, in B3PW simulations, a symmetrical STO perovskite (001) slab (Figure 21) [122,124,125] was exploited. This STO perovskite (001) substrate incorporated eleven alternating TiO_2 and SrO layers as well as a supercell formed from 28 atoms (Figure 21) [122–126].

As a following step, between one and 10 alternating PbO as well as TiO_2 layers from both sides of the STO perovskite (001) substrate (Figure 21) [122–126] were symmetrically augmented. Consequently, the biggest number of atoms in B3PW STO/PTO (001) heterostructure simulations was equal to 78 [122–126]. The respective formula for the 78-atom-unit cell is equal to $Sr_5Pb_{10}Ti_{16}O_{47}$. In B3PW computations, the STO/PTO (001) heterostructure joint lattice constant for the thickest calculated interface (Figure 21) was refined. The B3PW-simulated STO/PTO (001) heterostructure joint lattice constant is equivalent to 3.91 Å [122–126].

In B3PW simulations, the shifts of atoms Δz along the z-axis were computed using equation (4) [122–126]. The TiO_2-terminated upper-layer displacement Δz (-5.95% of a_0) of the 11-layer STO (001) substrate is illustrated in Figure 22 ($x = 0$). The B3PW-simulated inward relaxation magnitude (Δz) of the augmented PTO perovskite (001) thin film depends from the number of augmented layers. Namely, the relaxation magnitude Δz is equal to (-6.01; -7.76; -6.97; -8.25; -7.26; -8.38; -7.34; -8.54; -7.42; -8.54) (% of a_0) for the number of PTO (001) layers ranging from $x = 1$ to $x = 10$, respectively (Figure 22).

For PbO as well as TiO_2 terminations of the augmented PTO perovskite (001) thin film, the absolute value of the atomic relaxation magnitude (Δz) increases as a function of the augmented layers number (Figure 22). The absolute values of atomic displacements (Δz) for the TiO_2-terminated augmented PTO perovskite (001) thin film are, in all cases, larger than for the PbO-terminated augmented PTO (001) thin film (Figure 22).

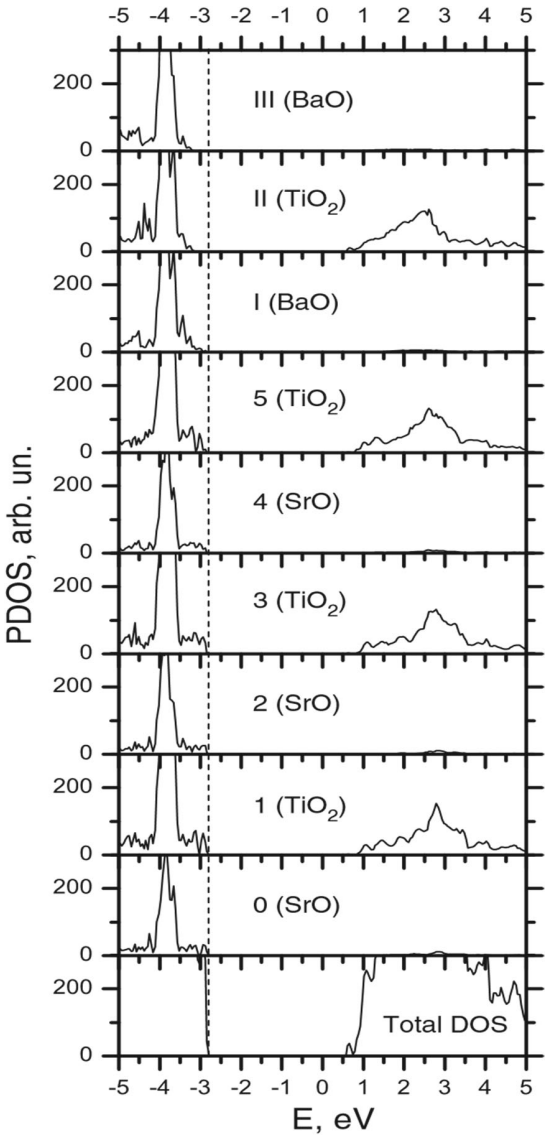

Figure 18. B3PW-simulated layer-by-layer design DOS for 3-UC-thick STO/BTO (001) interface [125].

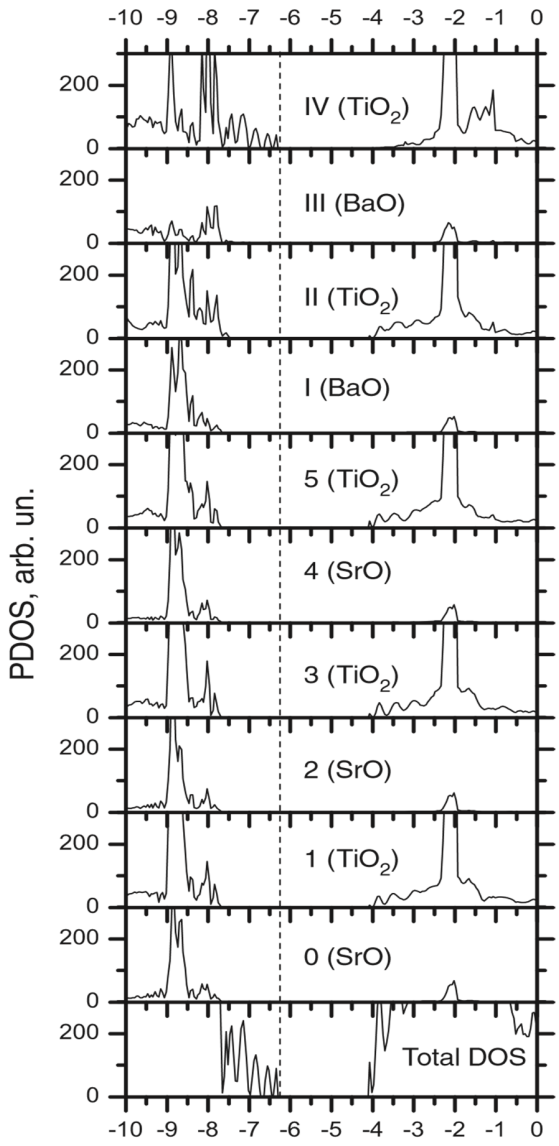

Figure 19. B3PW-simulated layer-by layer-design DOS for 4-UC-thick STO/BTO (001) interface [125].

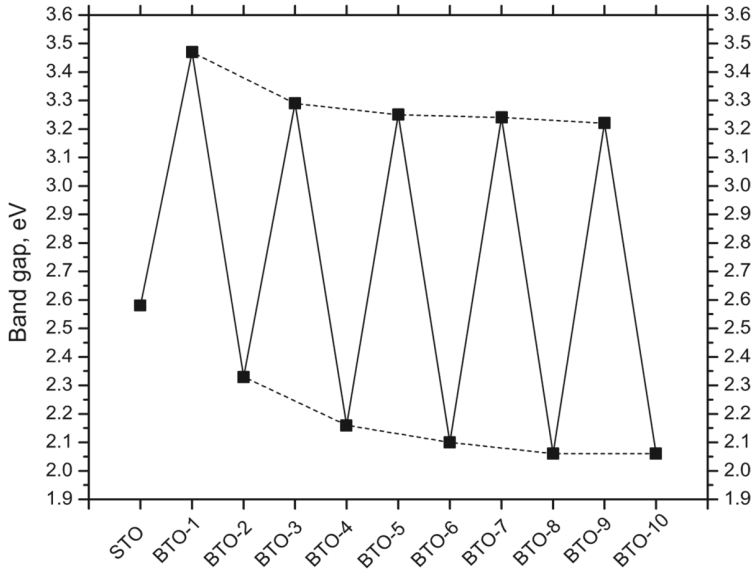

Figure 20. B3PW-simulated optical band gaps for the STO/BTO (001) interfaces. The number of augmented BTO layers on the STO (001) substrate range is (x = 0–10) [125].

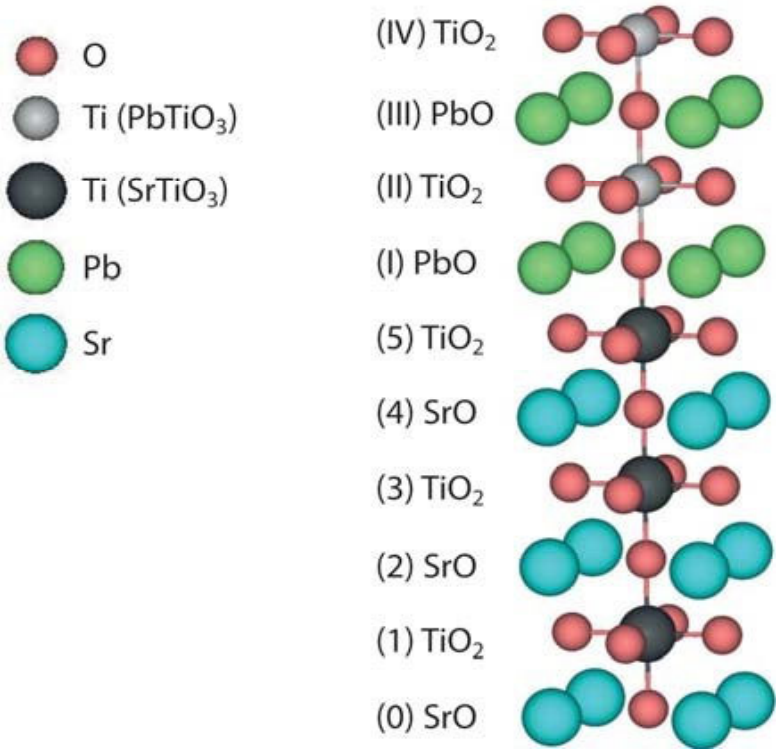

Figure 21. Illustration of B3PW-simulated STO/PTO (001) interface. The 11-layer STO perovskite (001) substrate is augmented, from both sides, by 10 PTO perovskite (001) layers [125].

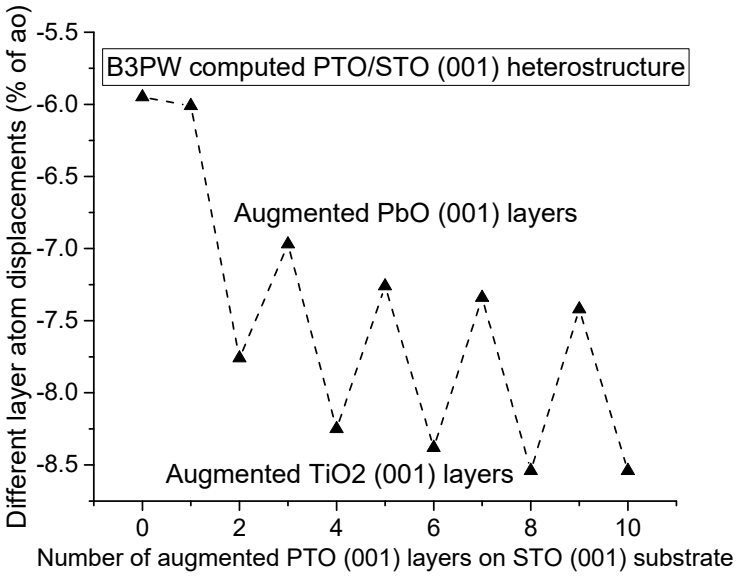

Figure 22. B3PW-simulated top layer atom displacement sizes Δz for the 11 layer STO perovskite (001) substrate upper layer (x = 0) as well as 10 augmented PTO (001) layers (x = 1–10) [122–126].

Figure 22 illustrates the electronic charge reallocation along the STO/PTO (001) heterostructure with regards to the pristine STO perovskite and PTO perovskite (001) slabs [125,126]. The electronic charge density redistribution is determined as the electronic density on the STO/PTO (001) interface minus the amount of the electron densities in the STO perovskite (001) substrate as well as PTO perovskite thin film (001) slabs (Figure 22). These B3PW simulation results are depicted in Figure 23 for both three- as well as four-UC-thick STO/PTO (001) interfaces [125,126]. Figure 23 demonstrates that the key distortions

happen at the STO/PTO (001) interfaces and are triggered by the compensation of the slab surface effects [125,126].

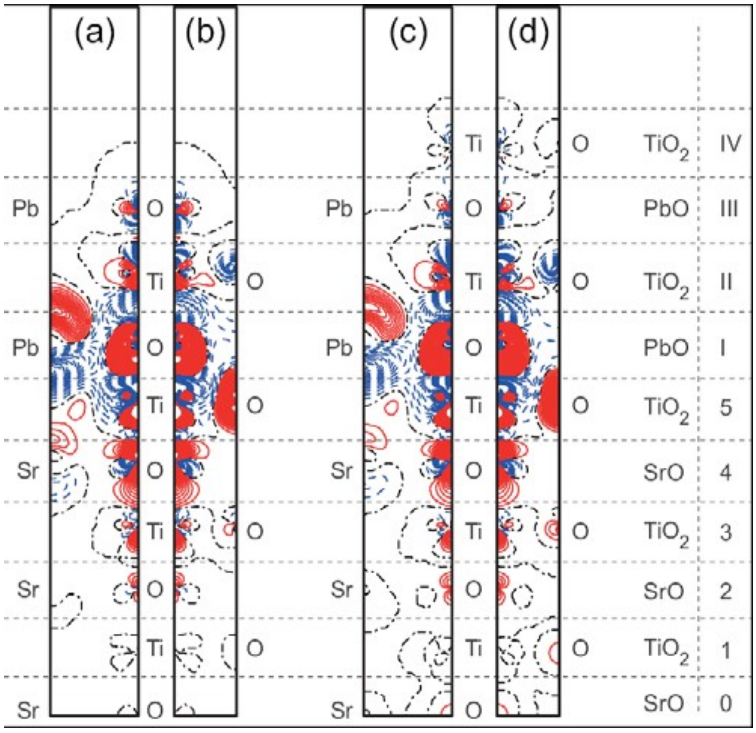

Figure 23. B3PW-simulated electron difference charge density maps of STO/PTO (001) heterostructures: (**a**) (110) cross-section of N_{PTO} = 3. (**b**) (100) cross-section of N_{PTO} = 3. (**c**) (110) cross-section of N_{PTO} = 4. (**d**) (100) cross-section of N_{PTO} = 4. Blue dashed, red solid as well as black dash–dot isolines describes negative, positive as well as 0 values for the difference charge density. Isodensity lines were illustrated in the interval from −0.025 to +0.025*e* Å^{-3} with a small increment equal to 0.0005*e* Å^{-3} [125].

B3PW-simulated DOS results, which were collected layer by layer for all orbitals of Sr, Pb as well as Ti atoms of 3 and 4 UC thick STO/PTO (001) heterostructures, are illustrated in Figures 24 and 25 [125,126]. In comparison with the ABO perovskite bulk, the VB top of the STO/PTO (001) heterostructure contains mostly O2p orbitals. On the contrary, the CB bottom of the STO/PTO (001) heterostructures mostly contains Ti3*d* atomic orbitals [125,126].

The B3PW-simulated band gap of the PbO-terminated PTO perovskite (001) thin film augmented on the 11-layer STO perovskite (001) substrate for one augmented layer (x = 1) is equal to 3.45 eV (Figures 25 and 26) [125,126]. The PbO-terminated PTO perovskite on the STO perovskite (001) substrate augmented (001) thin film band gaps, containing three, five, seven as well as nine layers are equal to 3.25, 3.08, 2.99 and 2.94 eV (Figures 26 and 27) [125,126]. B3PW-simulated band gaps for the TiO_2-terminated PTO perovskite (001) thin films, augmented on the STO perovskite 11-layer (001) substrate, for two, four, six, eight and 10 augmented layers are equal to 3.18, 3.17, 3.05, 2.99 and 2.93 eV (Figures 26 and 27) [125,126].

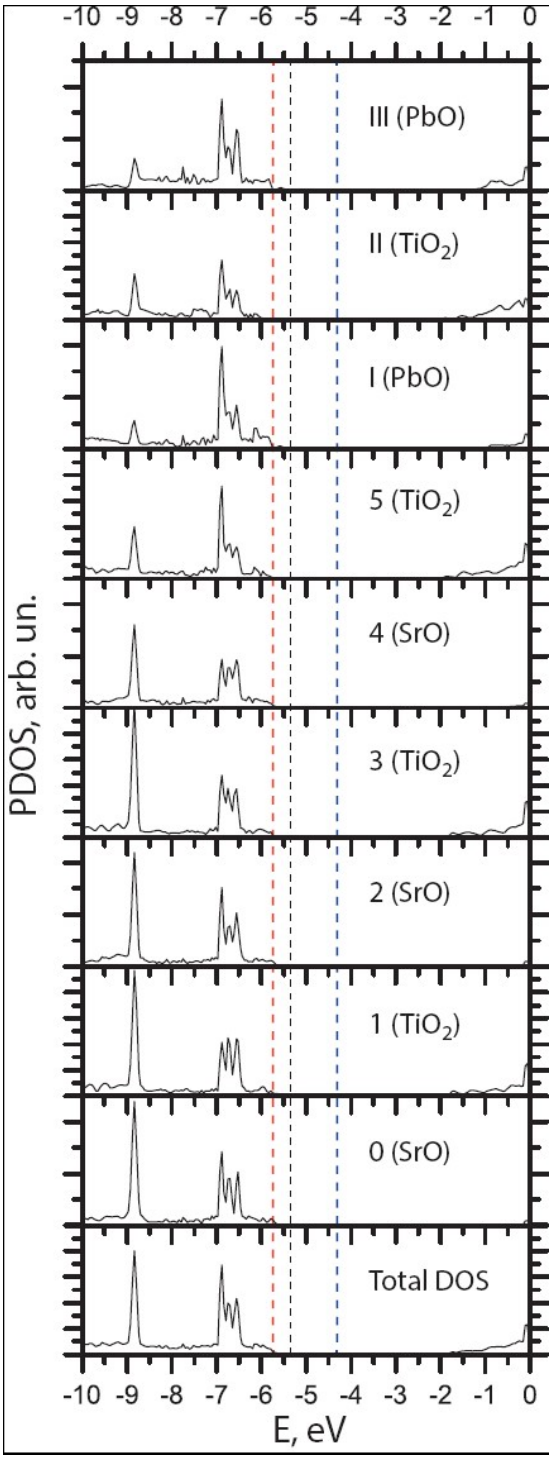

Figure 24. B3PW-simulated layer-by-layer projected DOS for the 3-UC-thick STO/PTO (001) heterostructure [125].

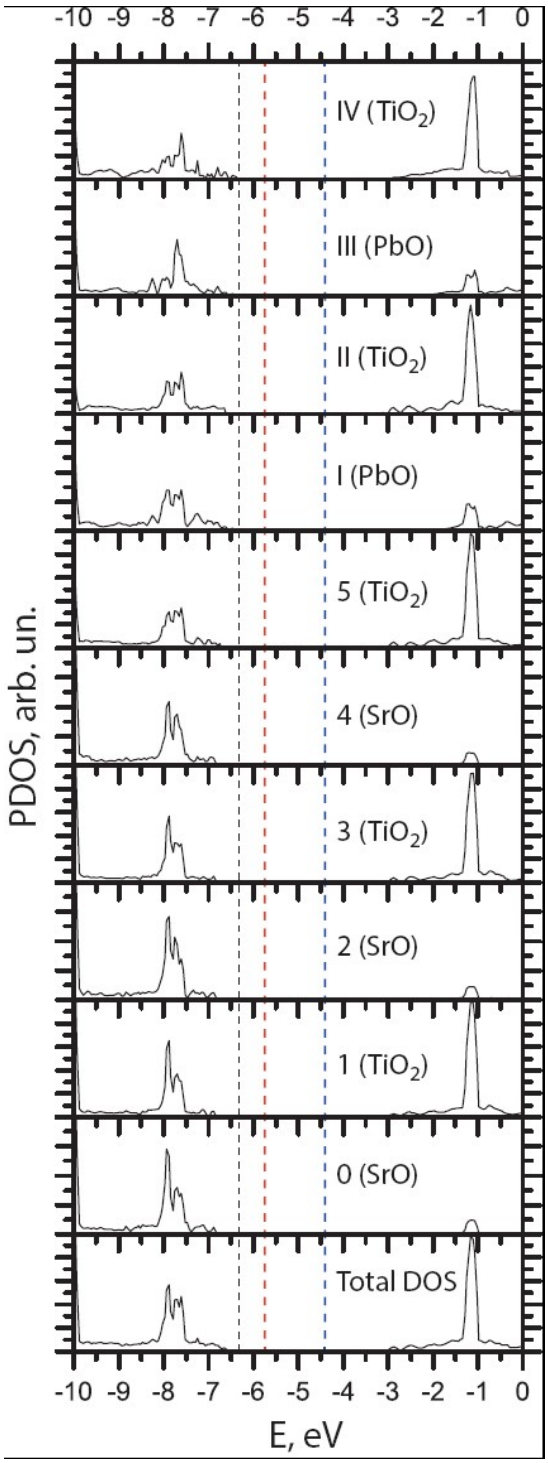

Figure 25. B3PW-simulated layer-by-layer projected DOS for the 4-UC-thick STO/PTO (001) heterostructure [125].

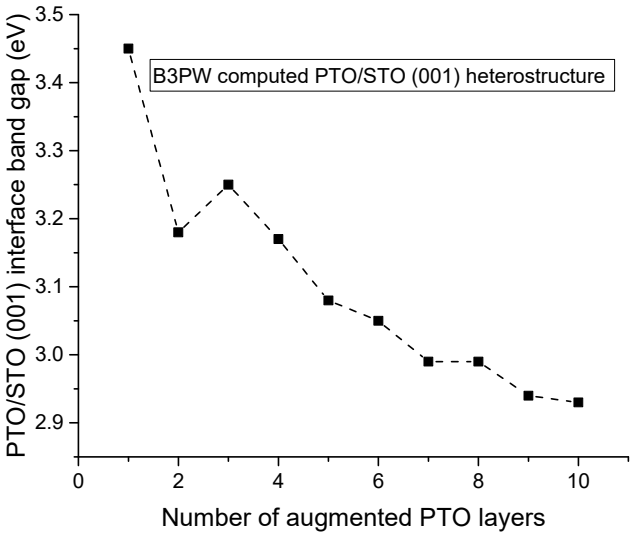

Figure 26. B3PW-simulated band gaps (in eV) for the STO/PTO (001) interfaces. Number of augmented PTO perovskite (001) layers changes in the range (x = 1–10) [125].

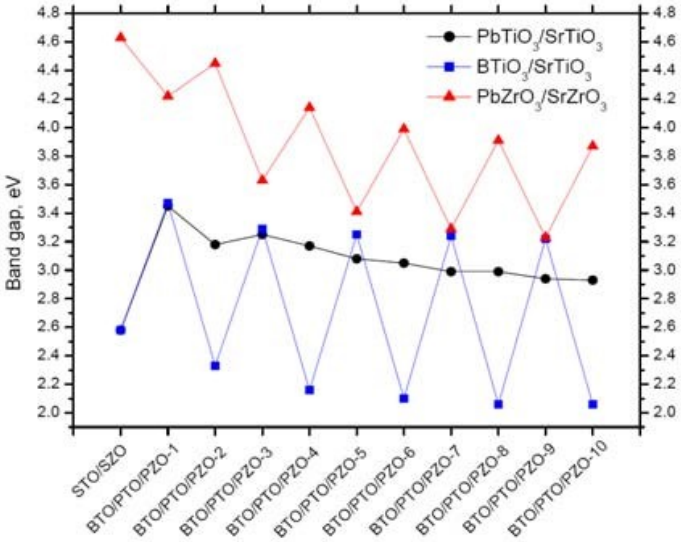

Figure 27. B3PW-simulated band gaps (in eV) for the STO/PTO (001) heterostructures as a function of augmented PTO (001) layers (x = 1–10). B3PW-simulated band gaps for STO/BTO as well as SZO/PZO (001) interfaces are discussed for comparison [125].

3.5. B3PW-Simulated SZO/PZO (001) Heterostructures

The B3PW simulations for the SZO/PZO (001) interfaces, using the same model as for the related STO/BTO as well as STO/PTO (001) heterostructures [122–126] were performed. In B3PW simulations, the SZO perovskite (001) substrate also contained 11 layers. The SZO (001) substrate was terminated from both sides with ZrO_2 layers [122–126]. Next, symmetrically to both sides of the SZO (001) substrate, were attached a pair of PZO (001) layers [123,125,126]. At the final stage, the deposited PZO (001) thin film was extended to 10 layers on both sides of the SZO (001) substrate [123,125,126].

As a following step, with the aim to determine the degree of the electronic charge density redistribution, the performance of the electronic charge density near the (001) heterostructures (Figure 28) [123,125,126] was inspected. B3PW simulation results were matched up to the isolated BTO, PZO, STO as well as SZO (001) slabs (Figure 28). According to the difference in electron charge density plots, illustrated in Figure 28, the main electron distortion happens at the (001) interface [123,125,126]. These distortions happen

as a result of the compensation for the B3PW-simulated surface effects of the (001) slabs (Figure 28) [123,125,126].

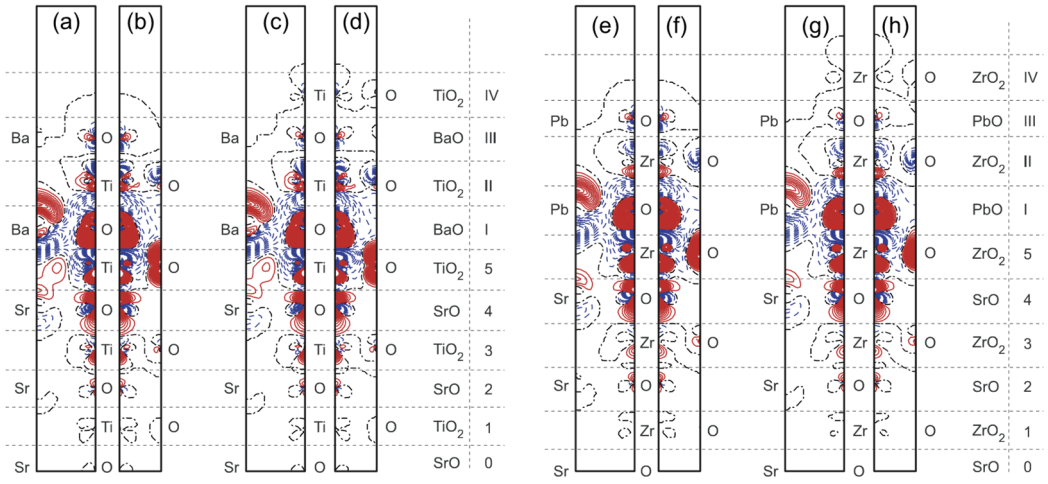

Figure 28. B3PW-computed difference in electron charge density plots simulated for the STO/PTO as well as SZO/PZO (001) heterostructures. (**a**) (110) cross-section for N_{BTO} = 3. (**b**) (100) cross-section for N_{BTO} = 3. (**c**) (110) cross-section for N_{BTO} = 4. (**d**) (100) cross-section for N_{BTO} = 4. (**e**) (110) cross-section for N_{PZO} = 3. (**f**) (100) cross-section for N_{PZO} = 3. (**g**) (110) cross-section for N_{PZO} = 4. (**h**) (100) cross-section for N_{PZO} = 4. Blue dashed, red solid as well as black dash–dot isolines defines negative, positive as well as 0 values for the difference charge density. Isodensity curves are illustrated from −0.025 to +0.025*e* Å^{-3} with an increment of 0.0005*e* Å^{-3} [125].

The DOS-projected layer by layer upon all orbitals of the Sr, Ba, Pb, Ti, O as well as Zr atoms of the STO/BTO and SZO/PZO (001) interfaces [123,125,126] was meticulously inspected. Just as for the ABO perovskite bulk, the VB top was comprised of O 2*p* orbitals. On the contrary, the CB band bottom was composed mostly of Ti *3d* and Zr *4d* orbitals [123,125,126]. Additionally, Ti-O as well as Zr-O hybridization are pronounced clearly. For the BaO-terminated STO/BTO as well as ZrO_2-terminated SZO/PZO (001) interfaces, a surplus of electron density relocations was gained, due to an increase in the number of occupied levels, generating a rise of the enlarged band gap (Figure 29) [123,125,126]. On the other hand, the PbO- as well as TiO_2-terminated (001) interfaces underwent a shortage of electron density (Figure 29). This displaced the number of filled levels downwards. The band gaps of the SZO/PZO as well as STO/BTO (001) heterostructures thereby were reduced (Figure 29).

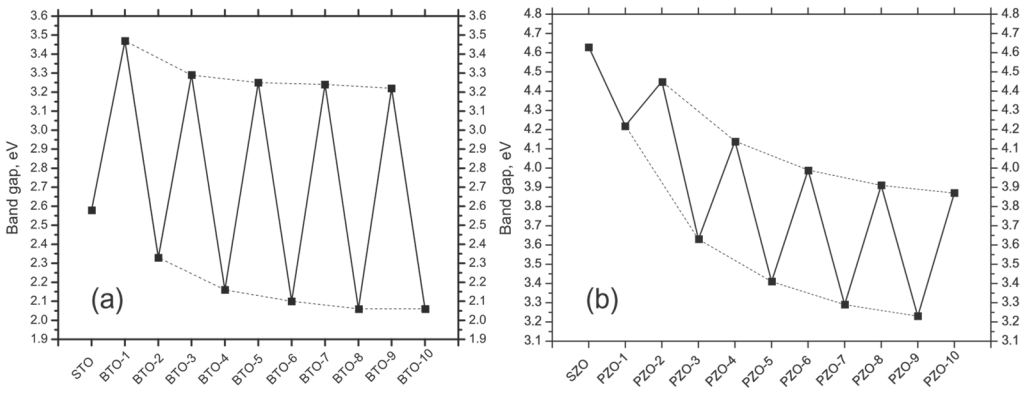

Figure 29. B3PW-computed band gaps (in eV) for the (**a**) STO/BTO as well as (**b**) SZO/PZO (001) interfaces. The deposited BTO or PZO layer number varies in the range (x = 1–10) [125].

3.6. B3PW Simulations of Oxygen Vacancies in ABO Perovskite Bulk and on Their (001) Surfaces

B3PW-simulation results, dealing with the atomic displacement magnitudes nearby the bulk as well as (001) surface oxygen vacancies in the STO, BTO, PTO and SZO perovskites are collected in Table 9 [64,107,135,170,181–185]. According to B3PW simulations all B (Ti or Zr) atoms always are repelled from the bulk as well as (001) surface oxygen vacancies in all four ABO perovskites (Table 9). The repulsion magnitudes of the B atoms on the STO, PTO and SZO (001) surfaces (+14.0, +9.98, +9.17% of a_0) are significantly larger than the respective bulk B atom displacement magnitudes (+7.76, +1.63, +3.68% of a_0) (Table 9). The single exception from this systematic trend is very small repulsion of the BTO perovskite Ti atom (+0.1% of a_0) from the oxygen vacancy on the BTO perovskite (001) surface in comparison with the bulk (+1.06% of a_0) (Table 9) [64,107,135,170,181–185].

Table 9. B3PW-simulated the three nearest-neighbor atom displacement magnitudes near the bulk as well as the (001) surface oxygen vacancy (% of a_0) in ABO perovskites [64,107,135,170,181–185].

Simulated Properties	**STO**	**BTO**	**PTO**	**SZO**
Functional	B3PW	B3PW	B3PW	B3PW
ABO lattice constant (Å)	3.904	4.008	3.936	4.163
Bulk *F*-center in ABO perovskites				
B atom displac. magnitude	+7.76	+1.06	+1.63	+3.68
O atom displac. magnitude	−7.79	−0.71	−0.88	−2.63
A atom displac. magnitude	+3.94	−0.08	−2.58	+0.46
F-center on ABO perovskite (001) surface				
B atom displac. magnitude	+14.0	+0.1	+9.98	+9.17
O atom displac. magnitude	−8.0	−1.4	−5.58	−4.16
A atom displac. magnitude	-	+1.0	-	+7.68

The second-closest to the *F*-center oxygen atoms, both in the ABO perovskite bulk as well as on their (001) surfaces, in all cases, are moved closer to the oxygen vacancy (Table 9). Numerically, the second-closest to the *F*-center oxygen atoms, in the STO, BTO, PTO, and SZO perovskites are shifted towards the bulk oxygen vacancy by (−7.79, −0.71, −0.88, −2.63% of a_0) (Table 9) [64,107,135,170,181–185]. According to performed B3PW simulations, the second-nearest-neighbor O atoms on the STO, BTO, PTO, and SZO perovskite (001) surfaces are shifted towards the (001) surface's *F*-center (−8.0, −1.4, −5.58, −4.16% of a_0, respectively) even more strongly than in the bulk case (Table 9).

The neutral oxygen atom willingly creates an ion with a charge equal to $-2e$ (Table 10). In B3PW simulations, the O atom charges in the perfect STO, BTO, PTO, and SZO perovskites are substantially smaller than their ionic charges ($-2e$). They are equal to ($-1.407e$; $-1.388e$; $-1.232e$; $-1.351e$), respectively (Table 10). Interior the oxygen vacancies in the STO, BTO, PTO, and SZO perovskite bulk ($-1.10e$; $-1.103e$; $-0.85e$; $-1.25e$) are confined to a smaller amount of the electron charge (Table 10 and Figure 30). It is worth noticing that, inside the BTO and SZO perovskite (001) surface oxygen vacancies ($-1.052e$ and $-1.10e$), are localized even less electron charge than inside the related bulk oxygen vacancies (Table 10 and Figure 31). B3PW-simulated difference in electron charge density maps for the oxygen vacancy in the SZO perovskite bulk and on its (001) surface are illustrated in Figures 30 and 31.

B3PW-simulated formation energies of the bulk oxygen vacancies in the STO, BTO, PTO, and SZO perovskites are equal to 7.10, 10.30, 7.82, and 7.55 eV (Table 10 and Figure 32). The oxygen vacancy formation energies on the STO, BTO, PTO, and SZO perovskite (001)

surfaces (6.22, 10.20, 5.99, and 7.52 eV, respectively) are even smaller than in their bulk (Table 10 and Figure 32).

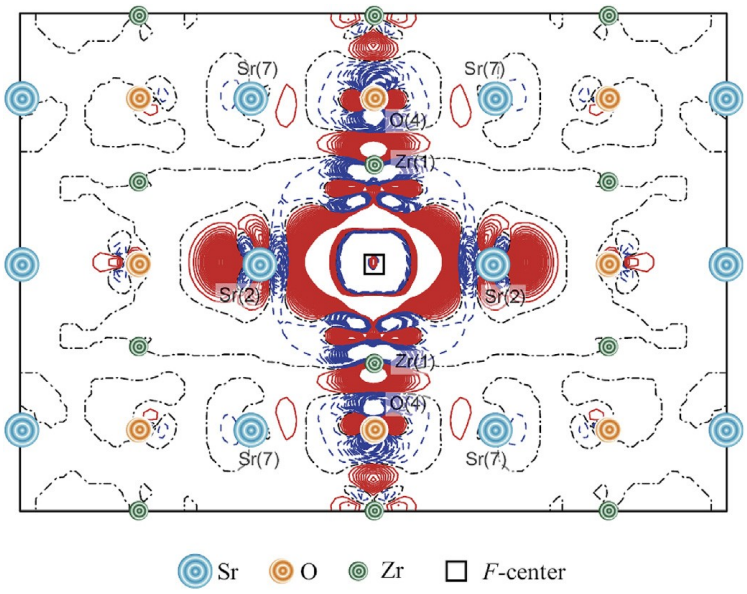

Figure 30. B3PW-simulated (110) cross-section of the difference in electron charge density maps $\Delta\rho(\mathbf{r})$ for the oxygen vacancy in the SZO perovskite bulk [64,107,135,170,181–185]. Dash–dot isolines represent the 0 level. Dashed isolines represent the decrease in the $\Delta\rho(\mathbf{r})$, whereas the solid lines represent its increase [170].

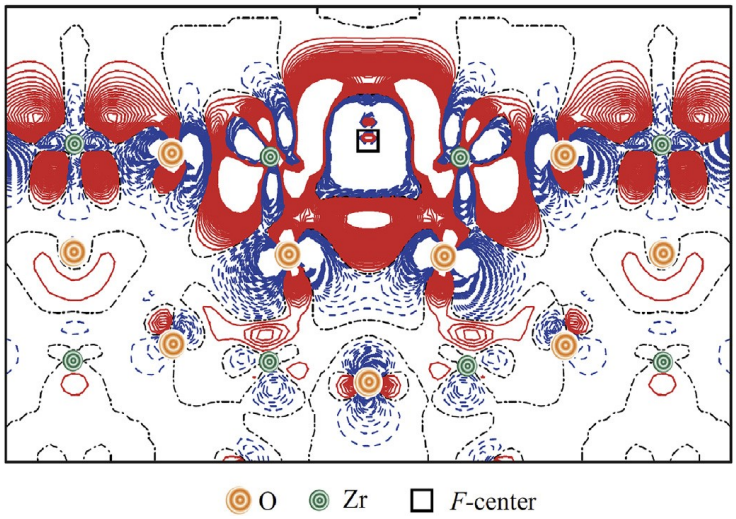

Figure 31. B3PW-simulated difference in electron charge density map for the ZrO_2-terminated SZO perovskite (001) surface, which contains the oxygen vacancy, in the cross-section alongside the (010) plane [64,107,135,170,181–185]. Dashed lines indicate the shortage of electron density. The full lines indicate the excess of electron density. The increment magnitude in B3PW simulations is equal to $0.05e$ a.u.^{3} [170].

Table 10. B3PW-simulated bulk and (001) surface oxygen vacancy atomic and electronic structure in STO, BTO, PTO, and SZO perovskites [64,107,135,170,181–185].

Simulated Properties	**STO**	**BTO**	**PTO**	**SZO**
Functional	B3PW	B3PW	B3PW	B3PW
Oxygen vacancy in the STO, BTO, PTO, and SZO perovskite bulk				
O atom ionic charge (*e*)	−2.0	−2.0	−2.0	−2.0
O charge in ABO matrix (*e*)	−1.407	−1.388	−1.232	−1.351
Oxygen vacancy charge (*e*)	−1.10	−1.103	−0.85	−1.25
O vac. format. energy (eV)	7.10	10.30	7.82	7.55
Band gap with *F*-cent. (eV)	3.63	3.58	2.87	5.07
F-center under CB (eV)	0.69	0.23	0.96	1.12
Oxygen vacancy on the STO, BTO, PTO, and SZO (001) surface				
Oxygen vacancy charge (*e*)	-	−1.052	-	−1.10
O vac. format. energy (eV)	6.22	10.20	5.99	7.52
F-center under CB (eV)	0.25	0.07	0.71	0.93

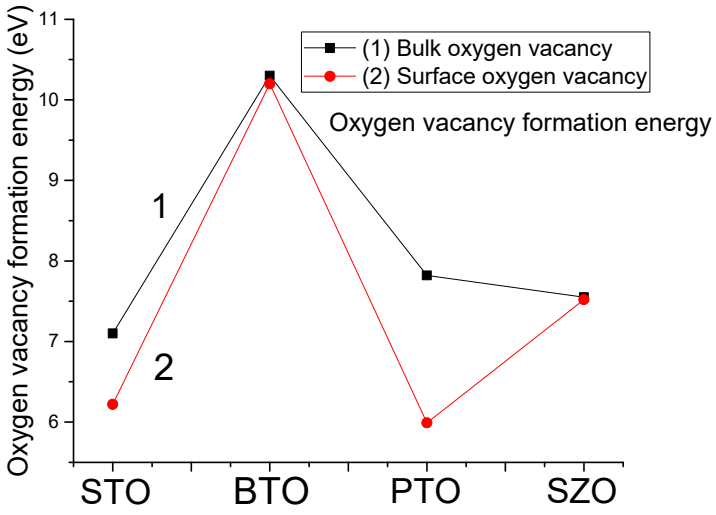

Figure 32. B3PW-simulated bulk (1) and surface (2) oxygen vacancy formation energies (eV) in the STO, BTO, PTO, and SZO perovskites [170].

Our B3PW-simulated bulk band gap breadth at the Γ-point, for the STO, BTO, PTO, and SZO perovskites, containing the oxygen vacancy, are equal to 3.63, 3.58, 2.87, 5.07 eV, respectively (Table 10 and Figure 33). The bulk oxygen vacancy induces the defect levels at the STO, BTO, PTO, and SZO perovskite band gaps (Table 10 and Figures 33 and 34). At the Γ-point, these defect levels for the STO, BTO, PTO, and SZO perovskites bulk are located 0.69, 0.23, 0.96, and 1.12 eV below the conduction band (CB) bottom (Table 10 and Figures 33 and 34). The (001) surface oxygen vacancy-induced defect levels, on the STO, BTO, PTO, and SZO perovskite (001) surfaces, at the Γ-point, are located even closer to the CB bottom (0.25, 0.07, 0.71, and 0.93 eV, respectively) (Table 10 and Figures 33 and 34).

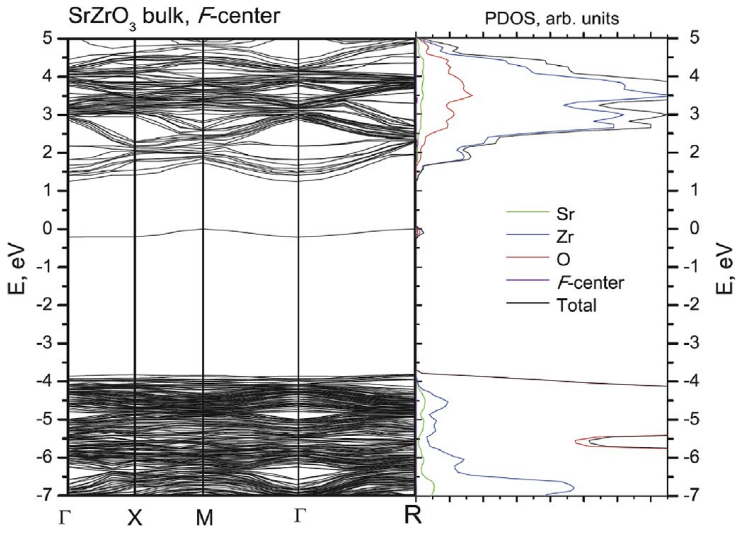

Figure 33. B3PW-simulated total as well as projected DOS, and band structure for the SZO perovskite bulk containing the single oxygen vacancy [170].

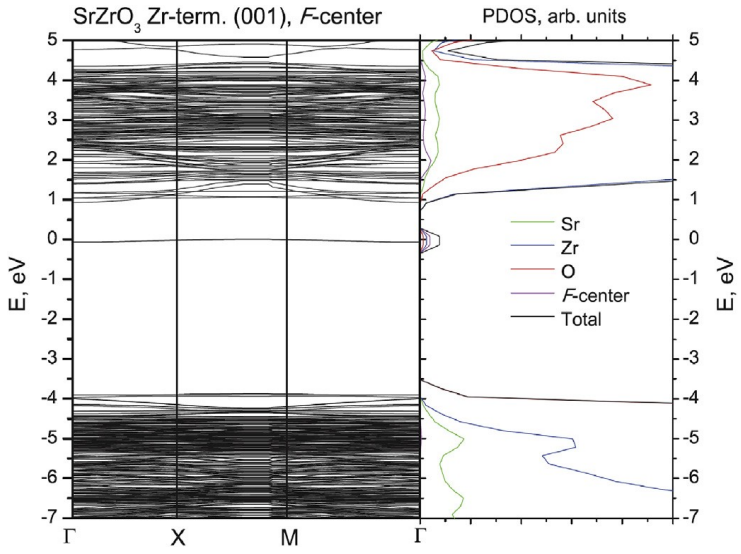

Figure 34. B3PW-simulated total as well as projected DOS, and band structure for the ZrO_2-terminated SZO perovskite (001) surface containing the single oxygen vacancy [170].

4. Conclusions

We discuss the performed B3LYP and B3PW simulations dealing with ABO perovskite (001) surfaces, interfaces as well as oxygen vacancy defects therein, during the last quarter of century worldwide [1–3,45,46,53,63,64,74,78,79,104,106,109,171], specifically B3PW and B3LYP simulations for the BO_2- as well as AO-terminated (001) surfaces of STO, BTO, PTO, CTO, SZO, BZO, PZO, and CZO perovskites [1–3,45,46,53,63,64,74,78,79,104,106,109,171]. According to carried out B3PW and B3LYP-simulations, almost all upper-layer atoms on the BO_2- and AO-terminated ABO (001) surfaces shift inwards. The only two deviations from this systematic tendency are the upward shifts of O atoms on the TiO_2-terminated PTO perovskite (001) surface by (+0.31% of a_0), and also on the SrO-terminated STO (001) surface by an even larger displacement magnitude equal to (+0.84% of a_0) (Table 4). On the other hand, almost all ABO perovskite second-layer atoms relax upwards (Table 4). The single exception to this systematic trend is the O atom's inward relaxation on the SrO-terminated SZO (001) surface by a very small relaxation magnitude of (−0.05% of a_0) (Table 4). Finally, practically all third-layer atoms, once more, relax inwards (Table 4).

It is worth noting that it is possible to compare directly ab initio computed relaxed ABO perovskite (001) surface structures with available experimental data. For example, the B3PW-simulated SrO-terminated STO perovskite (001) surface rumpling *s* by Eglitis and Vanderbilt is equal to 5.66 percent of the bulk lattice constant [2]. It is in fair agreement with the LDA calculation result by Padilla and Vanderbilt (5.8% of a_0) [186], and the LDA result obtained by Lee et al., (7.7% of a_0) using the CASTEP computer code [101]. Also, Heifets et al. [50] got a rather similar result (8.2% of a_0) using a completely different classical shell model method. On the experimental side, the LEED and RHEED experiments performed by Bickel et al., (4.1 $\pm$ 2% of a_0) [187] and Hikita et al., (4.1% of a_0) [188] yielded slightly lower, but comparable results with theoretical ab initio calculations [2,50,101,186].

Another experimentally measurable parameter, which allow us to check the accuracy of ab initio calculations, is the interlayer distance Δd_{12} between the ABO perovskite (001) surface's first and second layer [187,188]. Nevertheless, it is important to note that LEED [187] (-5 ± 1) and RHEED [188] (2.6) experiments contradict each other. Namely, the LEED experiments performed by Bickel et al. [187] favor the contraction between the first and second layer of SrO-terminated STO (001) surface (-5 ± 1), whereas the RHEED experiments carried out by Hikita et al. [188] show expansion (2.6). In this case, ab initio calculations performed by different scientific groups worldwide, dealing with atomic relaxation of SrO-terminated STO (001) surfaces helped to resolve this contradiction between LEED [187] and RHEED [188] experiments. That is to say, the interlayer distance Δd_{12} simulated by Eglitis and Vanderbilt (-6.58) [2], by Padilla and Vanderbilt (-6.9) [186], Lee et al., (-8.6) [101] as well as by Heifets et al., (-8.6) [50] are in good agreement with each other as well as with LEED experiments (-5 ± 1) [187].

The B3LYP- and B3PW-simulated ABO perovskite (001) surface energies, using the CRYSTAL computer code, for both BO_2 and AO terminations, are comparable (Table 5). It is worth noting that, by means of a quite different semi-empirical shell model (SM), computed (001) surface energies by Heifets et al. [50] for BTO and STO perovskites are also comparable. Namely, according to classical SM simulations [50], the Ba-terminated BTO (001) surface energy (1.45 eV) is only very slightly larger than the Ti-terminated surface (1.40 eV). Also, for STO perovskite by means of SM [50], the Ti-terminated (001) surface energy of 1.37 eV is slightly larger than for Sr termination (1.33 eV).

Nevertheless, the largest B3LYP-simulated surface energy is for the ZrO_2-terminated CZO (001) surface (1.33 eV) [171]. In contrast, the smallest B3PW-simulated surface energy is for the TiO_2-terminated PTO (001) surface (0.74 eV) [1]. B3LYP and B3PW simulations in the ABO perovskites indicate a significant rise of the B-O chemical bond covalency nearby the BO_2-terminated (001) surfaces in comparison to their bulk [1–3,45,46,53,63,64,74,78,79,104,106,109,171]. Namely, for the STO, BTO, PTO, CTO, SZO, BZO, PZO, and SZO perovskites, the bulk B-O chemical bond covalency (+0.088*e*, +0.098*e*, +0.098*e*, +0.084*e*, +0.092*e*, +0.108*e*, +0.106*e*, +0.086*e*, respectively) soar near the BO_2-terminated (001) surface (0.118*e*, 0.126*e*, 0.114*e*, 0.114*e*, 0.114*e*, 0.132*e*, 0.116*e*, 0.102*e*, respectively). B3LYP- and B3PW-simulated ABO perovskite bulk Γ-Γ band gaps are decreased near their BO_2- and AO-terminated (001) surfaces.

We reviewed worldwide available B3PW simulations for the STO/BTO, STO/PTO, and SZO/PZO (001) interfaces. In B3PW simulations, the non-stoichiometric (001) heterostructures were considered. It is demonstrated that charge rearrangement in the region of the (001) interface unsubstantially influences the electronic structure. At the same time, the modification in the stoichiometry creates an important shift in the band edges. B3PW-simulated optical band gaps of the STO/BTO, STO/PTO, and SZO/PZO (001) interfaces mainly depend on the BO_2 or AO terminations of the upper layer of the augmented film.

The strengthening of the B-O chemical bond covalency near the STO/BTO, STO/PTO and SZO/PZO (001) interfaces in comparison to the BTO, PTO and SZO bulk were forecasted.

The displacement magnitudes of the nearest-neighbor atoms, around the (001) surface oxygen vacancy, in the ABO perovskites, usually, are larger than in their bulk. In the STO, BTO, PTO, and SZO perovskites, the electronic charge, ordinarily, is a lot better localized interior the bulk than the (001) surface oxygen vacancy. In the STO, BTO, PTO, and SZO perovskites, the (001) surface oxygen vacancy-induced defect levels are located closer to the conduction band bottom than in the bulk cases. Computed formation energy difference between the bulk and the (001) surface oxygen vacancies in the STO, BTO, PTO, and SZO perovskites triggers the oxygen vacancy segregation from the bulk towards the (001) surface.

Author Contributions: Conceptualization, R.J., J.P., A.I.P. and S.P.K.; methodology, R.I.E.; software, R.I.E.; validation, R.I.E., R.J., J.P., A.I.P. and S.P.K.; formal analysis, R.I.E., J.P., A.I.P., S.P.K. and R.J.; investigation, R.I.E., and R.J.; resources, S.P.K.; data curation, S.P.K. and R.J.; writing—original draft preparation, R.I.E., J.P., A.I.P., S.P.K. and R.J.; writing—review and editing, R.I.E., J.P., A.I.P., R.J. and S.P.K.; visualization, S.P.K., R.J. and R.I.E.; funding acquisition, R.I.E.; J.P., A.I.P., S.P.K. and R.J. All authors have read and agreed to the published version of the manuscript.

Funding: This study was funded by the Latvian Council of Science, grant number: LZP-2025/1-0342 to J.P. and R.I.E. S.P.K. acknowledges support from the National Academy of Science of Ukraine (Funding No. 0116U002067). S.P.K. thanks the funding from Simons Foundation, under the Contract NUMBER–0121U109816.

Data Availability Statement: No new data were created or analyzed in this study.

Conflicts of Interest: The authors declare no conflicts of interest.

References

1. Eglitis, R.I.; Vanderbilt, D. Ab initio calculations of $BaTiO_3$ and $PbTiO_3$ (001) and (011) surface structures. *Phys. Rev. B* **2007**, *76*, 155439.
2. Eglitis, R.I.; Vanderbilt, D. First-principles calculations of atomic and electronic structure of $SrTiO_3$ (001) and (011) surfaces. *Phys. Rev. B* **2008**, *77*, 195408. [CrossRef]
3. Eglitis, R.I.; Vanderbilt, D. Ab initio calculations of the atomic and electronic structure of $CaTiO_3$ (001) and (011) surfaces. *Phys. Rev. B* **2008**, *78*, 155420. [CrossRef]
4. Dawber, M.; Rabe, K.M.; Scott, J.F. Physics of thin-film ferroelectric oxides. *Rev. Mod. Phys.* **2005**, *77*, 1083–1130. [CrossRef]
5. Brik, M.G.; Ma, C.G.; Krasnenko, V. First-principles calculations of the structural and electronic properties of the cubic $CaZrO_3$ (001) surfaces. *Surf. Sci.* **2013**, *608*, 146–153.
6. Lazaro, S.D.; Longo, E.; Sambrano, J.R.; Beltrán, A. Structural and electronic properties of $PbTiO_3$ slabs: A DFT periodic study. *Surf. Sci.* **2004**, *552*, 149–159.
7. Hussain, M.K.; Paudel, R.; Kahdum, B.J.; Syrotyuk, S. Optoelectronic and structural properties of bulk cubic perovskite $RbTaO_3$ and surface (001) for optoelectronic and spintronics applications. *Mater. Chem. Phys.* **2024**, *327*, 129778.
8. Chun, H.J.; Lee, Y.; Kim, S.; Yoon, Y.; Kim, Y.; Park, S.C. Surface termination of $BaTiO_3$ (111) single crystal: A combined DFT and XPS study. *Appl. Surf. Sci.* **2022**, *578*, 152018. [CrossRef]
9. Derkaoui, I.; Achehboune, M.; Eglitis, R.I.; Popov, A.I.; Rezzouk, A. Overview of the Structure, Electronic and Optical Properties of the cubic and Tetragonal Phase of $PbTiO_3$ by Applying Hubbard Potential Correction. *Materials* **2023**, *16*, 4302. [CrossRef]
10. Eom, K.; Chung, B.; Oh, S.; Zhou, H.; Seo, J.; Oh, S.H.; Jang, J.; Choi, S.Y.; Choi, M.; Seo, I.; et al. Surface triggered stabilization of metastable charge ordered phase in $SrTiO_3$. *Nat. Commun.* **2024**, *15*, 1180. [CrossRef] [PubMed]
11. Arkhipov, N.A.; Shulga, P.D.; Burkovsky, R.G. Gibbs energy approach to the thermodynamical phase diagrams of $PbZrO_3$ and $PbHfO_3$. *Phys. Rev. B* **2025**, *111*, L180102.
12. Hussain, M.K.; Paudel, R.; Syrotyuk, S.A. A new half-metallic structure of the RbO and TaO_2 termination in the cubic perovskite $RbTaO_3$: For spintronics and optoelectronic applications. *J. Mater. Sci.* **2024**, *59*, 16604–16617. [CrossRef]
13. Castell, M.R. Scanning tunneling microscopy of reconstructions on the $SrTiO_3$ (001) surface. *Surf. Sci.* **2002**, *505*, 1–13. [CrossRef]
14. Derkaoui, I.; Achehboune, M.; Eglitis, R.I.; Popov, A.I.; Boukhoubza, I.; Kabatas, M.A.B.M.; Rezzouk, A. Influence of the Hubbard U correction on the Electronic Properties and Chemical Bands of the Cubic (Pm3m) phase of $SrTiO_3$ using GGA/PBE and LDA/CA-PZ Approximations. *Molecules* **2024**, *29*, 3081. [CrossRef]

15. Inerbaev, T.M.; Abuova, A.U.; Zakiyeva, Z.Y.; Abuova, F.U.; Mastrikov, Y.A.; Sokolov, M.; Gryaznov, D.; Kotomin, E.A. Effect of Rh Doping on Optical Absorption and Oxygen Evolution Reaction Activity on $BaTiO_3$ (001) Surfaces. *Molecules* **2024**, *29*, 2707. [CrossRef]
16. Kaptagay, G.A.; Satanova, B.M.; Abuova, A.U.; Konuhova, M.; Zakiyeva, Z.Y.; Tolegen, U.Z.; Koilyk, N.O.; Abuova, F.U. Effect of rhodium doping for photocatalytic activity of barium titanate. *Opt. Mater. X* **2025**, *25*, 100382.
17. Gao, H.; Hu, C. First-principles study on influences of surface and thickness on magnetic and ferroelectric properties of quasi-two-dimensional $BaTiO_3$ (001) ultrathin film doped with Ni at Ti site. *Surf. Interfaces* **2025**, *69*, 106759.
18. Wu, S.; Zhao, C.; He, C.; Dong, X.; Xu, H. A Ternary Reconstruction on the $SrTiO_3$ (001) surface. *J. Phys. Chem. Lett.* **2025**, *16*, 3741–3747.
19. Grigorjeva, L.; Millers, D.K.; Pankratov, V.; Williams, R.T.; Eglitis, R.I.; Kotomin, E.A.; Borstel, G. Experimental and theoretical studies of polaron optical properties in $KNbO_3$ perovskite. *Solid State Commun.* **2004**, *129*, 691–696. [CrossRef]
20. Hong, C.; Song, Z.; Lin, B.; Ran, P.; Wu, T.; Xie, X.; Jiang, C.; He, R.H. Controlling surface reconstruction of $SrTiO_3$ (100) with adhesive outgassing. *J. Phys. Chem. Sol.* **2024**, *184*, 111716. [CrossRef]
21. Hao, W.; Gu, M.; Tian, Z.; Fu, S.; Meng, M.; Zhang, H.; Guo, J.; Zhao, J. Separated Electron-Phonon and Phonon-Phonon Scattering Across Interface in Thin Film $LaCoO_3/SrTiO_3$. *Adv. Sci.* **2024**, *11*, 2305900. [CrossRef]
22. Wu, B.; Liu, X.; Wang, M.; Lu, P.; Wu, M.; Sun, Y.; Yan, D.; Shi, Y.; Sun, N.X.; Wang, F. Artificial design of anisotropic magnetoelectric effect in $Sr_2IrO_4/SrTiO_3$ superlattices. *Appl. Phys. Lett.* **2024**, *125*, 072903. [CrossRef]
23. Lyle, H.; Singh, S.; Magnano, E.; Nappini, S.; Bondino, F.; Yazdi, S.; Cuk, T. Assessing and Quantifying Thermodynamically Concomitant Degradation during Oxygen Evolution from Water on $SrTiO_3$. *ACS Catal.* **2023**, *13*, 8206–8218. [CrossRef]
24. Komijo, K.; Nakajima, N.; Fan, D.; Anspoks, A. Two-Metal-Edge Extended X-ray Absorption Fine Structure Analysis of Oxygen Octahedral Rotation in $SrTiO_3$ Using the Reverse Monte Carlo Method. *J. Synchrotron Rad.* **2025**, *32*, 1010–1016. [CrossRef] [PubMed]
25. Kato, S.; Nakajima, N.; Yasui, S.; Yasuhara, S.; Fu, D.; Adachi, J.; Nitani, H.; Takeichi, Y.; Anspoks, A. Dielectric response of $BaTiO_3$ Electronic States under AC Fields via Microsecond Time-Resolved X-ray Absorption Spectroscopy. *Acta Mater.* **2021**, *207*, 116681. [CrossRef]
26. Iniguez, J.; Vanderbilt, D. First-principles study of the temperature-pressure phase diagram of $BaTiO_3$. *Phys. Rev. Lett.* **2002**, *89*, 115503. [CrossRef] [PubMed]
27. Cohen, R.E. Origin of ferroelectricity in perovskite oxides. *Nature* **1992**, *358*, 136–138. [CrossRef]
28. Long, T.; Song, D.; Zhou, Y.; Yu, X.; Wang, X.; Li, C.; Chen, H.; Li, G.; He, F. Modulating Activity of Lattice Oxygen of ABO_3 Perovskite Oxides in Redox Reactions: A Review. *ACS Appl. Mater. Interfaces* **2025**, *17*, 20590–20612. [CrossRef]
29. Hasan, M.; Nasrin, S.; Islam, M.N.; Hossain, A.K.M.A. First-principles insights into the electronic, optical, mechanical, and thermodynamic properties of lead-free cubic ABO_3 [A = Ba, Ca, Sr; B = Ce, Ti, Zr] perovskites. *AIP Adv.* **2022**, *12*, 085327. [CrossRef]
30. Humayun, M.; Li, Z.; Israr, M.; Khan, A.; Luo, W.; Wang, C.; Shao, Z. Perovskite Type ABO_3 Oxides in Photocatalysis, Electrocatalysis, and Solid Oxide Fuel Cells: State of the Art and Future Prospects. *Chem. Rev.* **2025**, *125*, 3165–3241. [CrossRef]
31. Sharma, N.; Hernandi, K. The Emerging Career of Strontium Titanates in Photocatalytic Applications: A Review. *Catalysts* **2022**, *12*, 1619. [CrossRef]
32. Li, W.B.; Zhou, D.; Xu, R.; Wang, D.W.; Su, J.Z.; Pang, L.X.; Liu, W.F.; Chen, G.H. $BaTiO_3$-Based Multilayers with Outstanding Energy Storage Performance for High Temperature Capacitor Applications. *ACS Appl. Energy Mater.* **2019**, *2*, 5499–5505.
33. Zhao, S.; Shen, S.S.; Han, L.; Tian, B.C.; Li, N.; Chen, W.; Li, X.B. Ferroelectric perovskite $PbTiO_3$ for advanced photocatalysis. *Rare Met.* **2024**, *43*, 4038–4055.
34. Passi, M.; Pal, B. A review on $CaTiO_3$ photocatalyst: Activity enhancement methods and photocatalytic applications. *Powder Technol.* **2021**, *388*, 274–304.
35. Weston, L.; Janotti, A.; Cui, X.Y.; Himmetoglu, B.; Stampfl, C.; Walle, C.G.V. Structural and electronic properties of $SrZrO_3$ and $Sr(Ti,Zr)O_3$ alloys. *Phys. Rev. B* **2015**, *92*, 085201. [CrossRef]
36. Lin, M.H.; Wu, M.C.; Huang, C.Y.; Lin, C.H.; Tseng, T.Y. High-speed and localized resistive switching characteristics of double-layer $SrZrO_3$ memory devices. *J. Phys. D Appl. Phys.* **2010**, *43*, 295404. [CrossRef]
37. Lin, C.C.; Tu, B.C.; Lin, C.C.; Lin, C.H.; Tseng, T.Y. Resistive Switching Mechanisms of V-Doped $SrZrO_3$ Memory Films. *IEEE Electron Device Lett.* **2006**, *27*, 725–727.
38. Tsurunami, T.; Harigai, T.; Tanaka, D.; Nam, S.; Kakemoto, H.; Wada, S.; Saito, K. Artificial ferroelectricity in perovskite superlattices. *Appl. Phys. Lett.* **2004**, *85*, 5016–5018. [CrossRef]
39. Harigai, T.; Nam, S.; Kakemoto, H.; Wada, S.; Saito, K.; Tsurumi, T. Structural and dielectric properties of perovskite-type artificial superlattices. *Thin Solid Film.* **2006**, *509*, 13–17.
40. Jary, V.; Bohacek, P.; Mihokova, E.; Havlak, L.; Trunda, B.; Nikl, M. Photoluminescence properties of non-stoichiometric strontium zirconate powder phosphor. *Opt. Mater.* **2013**, *35*, 1019–1022. [CrossRef]

41. Qiao, Z.; Li, S.; Li, Y.; Xu, N.; Xiang, K. Structure, mechanical properties, and thermal conductivity of $BaZrO_3$ doped at the A-B site. *Ceram. Int.* **2022**, *48*, 12529–12536.
42. Wang, X.; Yang, F.; Yu, K.; Zhang, B.; Chen, J.; Shi, Y.; Yang, P.; He, L.; Li, H.; Liu, R.; et al. $PbZrO_3$-Based Anti-Ferroelectric Thin Films for High-Performance Storage: A Review. *Adv. Mater. Technol.* **2023**, *8*, 2202044.
43. André, R.S.; Zanetti, S.M.; Varela, J.A.; Longo, E. Synthesis by a chemical method and characterization of $CaZrO_3$ powders: Potential application as humidity sensors. *Ceram. Int.* **2014**, *40*, 16627–16634.
44. Prasanth, C.S.; Kumar, H.P.; Pazhani, R.; Solomon, S.; Thomas, J.K. Synthesis, characterization and microwave dielectric properties of nanocrystalline $CaZrO_3$ ceramics. *J. Alloys Compd.* **2008**, *464*, 306–309.
45. Heifets, E.; Eglitis, R.I.; Kotomin, E.A.; Maier, J.; Borstel, G. Ab initio modeling of surface structure for $SrTiO_3$ perovskite crystals. *Phys. Rev. B* **2001**, *64*, 235417. [CrossRef]
46. Eglitis, R.I.; Jia, R. Review of Systematic Tendencies in (001), (011) and (111) Surfaces Using B3PW as Well as B3LYP Computations of $BaTiO_3$, $CaTiO_3$, $PbTiO_3$, $SrTiO_3$, $BaZrO_3$, $CaZrO_3$, $PbZrO_3$ and $SrZrO_3$ Perovskites. *Materials* **2023**, *16*, 7623. [CrossRef] [PubMed]
47. Erdman, N.; Poeppelmeier, K.R.; Asta, M.; Warschkov, O.; Ellis, D.E.; Marks, L.D. The structure and chemistry of the TiO_2-rich surface of $SrTiO_3$ (001). *Nature* **2002**, *419*, 55–58. [CrossRef]
48. Costa-Amaral, R.; Gohda, Y. First-principles study of the adsorption of 3d transition metals on BaO- and TiO_2-terminated cubic-phase $BaTiO_3$ (001) surfaces. *J. Chem. Phys.* **2020**, *152*, 204701.
49. Morgan, M.T.; Taylor, N.T.; Hepplestone, S.P. The role of vacancies for surface stability of oxide perovskites. *Phys. Rev. B* **2025**, *112*, 045308.
50. Heifets, E.; Kotomin, E.A.; Maier, J. Semi-empirical simulations of surface relaxation for perovskite titanates. *Surf. Sci.* **2000**, *462*, 19–35. [CrossRef]
51. Setvin, M.; Reticcioli, M.; Poelzleitner, F.; Hulva, J.; Schmid, M.; Boatner, L.A.; Franchini, C.; Diebold, U. Polarity compensation mechanisms on the perovskite surface $KTaO_3$ (001). *Science* **2018**, *359*, 572–575.
52. Kotomin, E.A.; Eglitis, R.I.; Maier, J.; Heifets, E. Calculations of the atomic and electronic structure for $SrTiO_3$ perovskite thin films. *Thin Solid Film.* **2001**, *400*, 76–80.
53. Eglitis, R.I.; Heifets, E.; Kotomin, E.A.; Maier, J.; Borstel, G. First-principles calculations of perovskite thin films. *Mater. Sci. Semicond. Process.* **2002**, *5*, 129–134. [CrossRef]
54. Ellinger, F.; Shafiq, M.; Ahmad, I.; Reticcioli, M.; Franchini, C. Small polaron formation on the Nb-doped $SrTiO_3$ (001) surface. *Phys. Rev. Mater.* **2023**, *7*, 064602. [CrossRef]
55. Krainyukova, N.V.; Hamalii, V.O.; Peschanskii, A.V.; Popov, A.I.; Kotomin, E.A. Low temperature structure transformations on the (001) surface of $SrTiO_3$ single crystals. *Low Temp. Phys.* **2020**, *46*, 740–750. [CrossRef]
56. Chang, Y.J.; Phark, S.H. Atomic-scale visualization of initial growth of perovskites on $SrTiO_3$ (001) using scanning tunneling microscope. *Curr. Appl. Phys.* **2017**, *17*, 640–656. [CrossRef]
57. Eglitis, R.I. Comparative ab initio calculations of $SrTiO_3$ and $CaTiO_3$ polar (111) surfaces. *Phys. Status Solidi B* **2015**, *252*, 635–642.
58. Wang, Y.; Zhang, Z.; Wang, Y.; Doan, E.; Yuan, L.; Tang, W.; Yang, K. First-principles investigation of structural, electronic, and energetic properties of $BaSnO_3$ (001) surfaces. *Vacuum* **2023**, *212*, 111977.
59. Barret, N.; Dionot, J.; Martinotti, D.; Salje, E.K.H.; Mathieu, C. Evidence of surface anomaly during the cubic-tetragonal phase transition in $BaTiO_3$ (001). *Appl. Phys. Lett.* **2018**, *113*, 022901.
60. Chen, P.; Xu, Y.; Wang, N.; Oganov, A.R.; Duan, W. Effects of ferroelectric polarization on surface phase diagram: Evolutionary algorithm study of the $BaTiO_3$ (001) surface. *Phys. Rev. B* **2015**, *92*, 085432.
61. Borstel, G.; Eglitis, R.I.; Kotomin, E.A.; Heifets, E. Modelling of defects and surfaces in perovskite ferroelectrics. *Phys. Status Solidi B* **2003**, *236*, 253–264. [CrossRef]
62. Eglitis, R.I.; Kleperis, J.; Purans, J.; Popov, A.I.; Jia, R. Ab initio calculations of $CaZrO_3$ (011) surfaces: Systematic trends in polar (011) surface calculations of ABO_3 perovskites. *J. Mater. Sci.* **2020**, *55*, 203–217. [CrossRef]
63. Eglitis, R.I.; Purans, J.; Popov, A.I.; Bocharov, D.; Chekhovska, A.; Jia, R. Ab initio computations of O and AO as well as ReO_2, WO_2 and BO_2-terminated ReO_3, WO_3, $BaTiO_3$, $SrTiO_3$ and $BaZrO_3$ (001) surfaces. *Symmetry* **2022**, *14*, 1050. [CrossRef]
64. Eglitis, R.I.; Kruchinin, S.P. Ab initio calculations of ABO_3 perovskite (001), (011) and (111) nano-surfaces, interfaces and defects. *Mod. Phys. Lett.* **2020**, *34*, 2040057. [CrossRef]
65. Muff, S.; Fanciulli, M.; Weber, A.P.; Pilet, N.; Ristić, Z.; Wang, Z.; Plumb, N.C.; Radović, M.; Dil, J.H. Observation of a two-dimensional electron gas at $CaTiO_3$ film surfaces. *Appl. Surf. Sci.* **2018**, *432*, 41–45. [CrossRef]
66. Tian, H.; Mao, A.J.; Zhao, H.J.; Cui, Y.; Li, H.; Kuang, X.Y. Large polarization and dielectric response in epitaxial $SrZrO_3$ films. *Phys. Chem. Chem. Phys.* **2016**, *18*, 7680–7687. [CrossRef]
67. Enterkin, J.A.; Subramanian, A.K.; Russell, B.C.; Castell, M.R.; Poeppelmeier, K.R.; Marks, L.D. A homologous series of structures on the surface of $SrTiO_3$ (110). *Nat. Mater.* **2010**, *9*, 245–248.

68. Blaess, C.; Matzen, S.; Lin, H.; Magnan, H.; Moussy, J.P.; Rountree, C.L.; Mocuta, C.; Silly, M.G.; Plantevin, O.; Charra, F.; et al. Nitrogen Doping in Epitaxial Self-Oxidized $BaTiO_3$ Ferroelectric Thin Films. *J. Phys. Chem. C* **2025**, *129*, 3849–3861. [CrossRef]
69. Celik, F.A. Electronic structure of two-dimensional-layered $PbTiO_3$ perovskite crystal: An extended tight-binding study based on DFT. *Bull. Mater. Sci.* **2022**, *45*, 108.
70. Li, W.; Landis, C.M.; Demkov, A. Domain morphology and electro-optic effect in Si-integrated epitaxial $BaTiO_3$ films. *Phys. Rev. Mater.* **2022**, *6*, 095203.
71. Hwang, H.Y.; Iwasa, Y.; Kawasaki, M.; Keimer, B.; Nagaosa, N.; Tokura, Y. Emergent phenomena at oxide interfaces. *Nat. Mater.* **2012**, *11*, 103–113. [CrossRef]
72. Cord, B.; Courths, R. Photoemission study of $BaTiO_3$ (100) surfaces. *Surf. Sci.* **1985**, *152–153*, 1141–1146. [CrossRef]
73. Li, Y.X.; Gan, H.; Xu, B.; Zhang, H.X.; Shen, S.C.; Yin, Y.W.; Li, X.G. First-principles study on ferroelectricity in monolayer $BaTiO_3$. *Phys. Rev. B* **2025**, *111*, 214114.
74. Eglitis, R.I.; Purans, J.; Jia, R.; Kruchinin, S.P.; Wirth, S. Comparative B3PW and B3LYP calculations of ABO_3 (A = Ba, Sr, Pb, Ca; B = Sn, Ti, Zr) Neutral (001) and Polar (111) Surfaces. *Inorganics* **2025**, *13*, 100.
75. Everhardt, A.S.; Denneulin, T.; Grünebohm, A.; Shao, Y.T.; Ondrejkovic, P.; Zhou, S.; Domingo, N.; Catalan, G.; Hlinka, J.; Zuo, J.M.; et al. Temperature-independent giant dielectric response in transitional $BaTiO_3$ thin films. *Appl. Phys. Rev.* **2020**, *7*, 011402. [CrossRef]
76. Eglitis, R.I. Ab initio calculations of $CaZrO_3$, $BaZrO_3$, $PbTiO_3$, $SrTiO_3$ (001), (011) and (111) surfaces as well as their (001) interfaces. *Integr. Ferroelectr.* **2019**, *196*, 7–15.
77. Eglitis, R.; Purans, J.; Popov, A.I.; Jia, R. Systematic trends in $YAlO_3$, $SrTiO_3$, $BaTiO_3$, $BaZrO_3$ (001) and (111) surface ab initio calculations. *Int. J. Mod. Phys. B* **2019**, *33*, 1950390.
78. Eglitis, R.I.; Popov, A.I.; Jia, R.; Kruchinin, S.P.; Derkaoui, I.; Kabatas, M.A. B3LYP and B3PW computations of $BaSnO_3$ and $BaZrO_3$ perovskite (001) surfaces. *Low Temp. Phys.* **2024**, *50*, 905–910. [CrossRef]
79. Eglitis, R.I.; Popov, A.I. Systematic trends in (001) surface ab initio calculations of ABO_3 perovskites. *J. Saudi Chem. Soc.* **2018**, *22*, 459–468. [CrossRef]
80. Lin, C.; Foucher, A.C.; Ji, Y.; Curran, C.D.; Stach, E.A.; McIntosh, S.; Gorte, R.J. Intelligent Pt Catalysts Studied on High-Surface-Area $CaTiO_3$ Films. *ACS Catal.* **2019**, *9*, 7318–7327. [CrossRef]
81. Zitello, K.E.; Salvador, P.A.; Rohrer, G.S. Influence of surface orientation on the photochemical reactivity of $CaTiO_3$. *J. Am. Ceram. Soc.* **2020**, *103*, 4498–4506. [CrossRef]
82. Plaza, A.E.; Manca, N.; Bernini, C.; Marre, D.; Pellegrini, L. The role of etching anisotropy in the fabrication of freestanding oxide microstructures on $SrTiO_3$ (100), $SrTiO_3$ (110), and $SrTiO_3$ (111) substrates. *Appl. Phys. Lett.* **2021**, *119*, 033504. [CrossRef]
83. Dagdeviren, O.E.; Simon, G.H.; Zou, K.; Walker, F.J.; Ahn, C.; Altman, E.I.; Schwarz, U.D. Surface phase, morphology, and charge distribution transitions on vacuum and ambient annealed $SrTiO_3$ (100). *Phys. Rev. B* **2016**, *93*, 195303. [CrossRef]
84. Nylund, I.E.; Raeder, T.M.; Vullum, P.E.; Grande, T. Epitaxial (100), (110), and (111) $BaTiO_3$ films on $SrTiO_3$ substrates. A transmission electron microscopy study. *J. Appl. Phys.* **2021**, *129*, 095304. [CrossRef]
85. Landau, L. The Theory of Phase Transitions. *Nature* **1936**, *138*, 840–841. [CrossRef]
86. Rosander, P.; Fransson, E.; Österbacka, N.; Erhart, P.; Wahnström, G. Untangling the Raman spectra of cubic and tetragonal $BaZrO_3$. *Phys. Rev. B* **2025**, *111*, 064107. [CrossRef]
87. Yao, J.; Chen, T.; Wang, H.; Khan, M.; Tan, C.; Sun, Y.; Su, W.; Wang, H.; Wang, C. Stable cubic crystal structures and optimized thermoelectric performance of $SrTiO_3$—Based ceramics driven by entropy engineering. *J. Mater. Chem. A* **2022**, *10*, 24561–24572. [CrossRef]
88. Cai, J.; Lan, S.; Wei, B.; Qi, J.; Nan, C.W.; Lin, Y.H. Colossal permittivity in high-entropy $CaTiO_3$ ceramics by chemical bonding engineering. *Nat. Commun.* **2025**, *16*, 4008. [CrossRef]
89. Li, S.; Wang, Y.; Yang, M.; Xu, S.; Liu, M.; Li, Q.; Miao, J.; Guo, E.J.; Jin, K.; Gu, L.; et al. Ferroelectricity in Low-Permittivity $SrZrO_3$ Epitaxial Films. *Chem. Mater.* **2023**, *35*, 2967–2974. [CrossRef]
90. Dufor, P.; Maroutian, T.; Vallet, M.; Patel, K.; Chanthbouala, A.; Jacquemont, C.; Yedra, L.; Humbert, V.; Godel, F.; Xu, B.; et al. Ferroelectric phase transitions in epitaxial antiferroelectric $PbZrO_3$ thin films. *Appl. Phys. Rev.* **2023**, *10*, 021405. [CrossRef]
91. Hoat, D.M.; Silva, J.F.R.; Blas, A.M. First principles study of structural, electronic and optical properties of perovskites $CaZrO_3$ and $CaHfO_3$ in cubic phase. *Solid State Commun.* **2018**, *275*, 29–34. [CrossRef]
92. Zhen, C.; Ren, Z.; Kang, Y.; Wang, L.; Liu, G. $PbTiO_3$ Based Single-Domain Ferroelectric Photocatalysts for Water Splitting. *Acc. Mater. Res.* **2023**, *4*, 591–603.
93. Qian, W.; Wu, H.; Yang, Y. Ferroelectric $BaTiO_3$ Based Multi-Effects Coupled Materials and Devices. *Adv. Electron. Mater.* **2022**, *8*, 2200190. [CrossRef]
94. Bondo, H.; Shimitzu, T.; Aiura, Y.; Haruyama, Y.; Oka, K.; Nishihara, Y. Structure and electronic states on reduced $BaTiO_3$ (100) surface observed by scanning tunneling microscopy and spectroscopy. *J. Vac. Sci. Technol. B* **1996**, *14*, 1060–1063. [CrossRef]

95. Berlich, A.; Strauss, H.; Langheinrich, C.; Chassé, A.; Morgner, H. Surface termination of $BaTiO_3$ (001) single crystals: A combined electron spectroscopic and theoretical study. *Surf. Sci.* **2011**, *605*, 158–165. [CrossRef]
96. Padilla, J.; Vanderbilt, D. Ab initio study of $BaTiO_3$ surfaces. *Phys. Rev. B* **1997**, *56*, 1625. [CrossRef]
97. Heifets, E.; Dorfman, S.; Fuks, D.; Kotomin, E. Atomistic simulation of the [001] surface structure in $BaTiO_3$. *Thin Solid Film.* **1997**, *296*, 76–78.
98. Kimura, S.; Yamauchi, J.; Tsukada, M.; Watanabe, S. First-principles study on electronic structure of the (001) surface of $SrTiO_3$. *Phys. Rev. B* **1995**, *51*, 11049. [CrossRef] [PubMed]
99. Goniakowski, J.; Noguera, C. The concept of weak polarity: An application to the $SrTiO_3$ (001) surface. *Surf. Sci.* **1996**, *365*, L657–L662. [CrossRef]
100. Heifets, E.; Dorfman, S.; Fuks, D.; Kotomin, E.; Gordon, A. [001] Surface Structure in $SrTiO_3$—Atomistic Study. *Surf. Rev. Lett.* **1998**, *5*, 341–345. [CrossRef]
101. Cheng, C.; Kunc, K.; Lee, M.H. Structural relaxation and longitudinal dipole moment of $SrTiO_3$ (001) (1×1) surfaces. *Phys. Rev. B* **2000**, *62*, 10409.
102. Erdman, N.; Warschkov, O.; Asta, M.; Poeppelmeier, K.R.; Ellis, D.E.; Marks, L. Surface Structures of $SrTiO_3$ (001): A TiO_2-rich Reconstruction with a c(4×2) Unit Cell. *J. Am. Chem. Soc.* **2003**, *125*, 10050–10056. [CrossRef] [PubMed]
103. Johnston, K.; Castell, M.R.; Paxton, A.T.; Finnis, M.W. $SrTiO_3$ (001) (2×1) reconstructions. First-principles calculations of surface energy and atomic structure compared with scanning tunneling microscopy images. *Phys. Rev. B* **2004**, *70*, 085415.
104. Piskunov, S.; Kotomin, E.A.; Heifets, E.; Maier, J.; Eglitis, R.I.; Borstel, G. Hybrid DFT calculations of the atomic and electronic structure for ABO_3 perovskite (001) surfaces. *Surf. Sci.* **2005**, *575*, 75–88. [CrossRef]
105. Wang, Y.X.; Arai, M.; Sasaki, T.; Wang, C.L. First-principles study of the (001) surface of cubic $CaTiO_3$. *Phys. Rev. B* **2006**, *73*, 035411.
106. Eglitis, R.I. First-principles calculations of $BaZrO_3$ (001) and (011) surfaces. *J. Phys. Condens. Matter* **2007**, *19*, 356004. [CrossRef]
107. Kotomin, E.A.; Piskunov, S.; Zhukovskii, Y.F.; Eglitis, R.I.; Gopejenko, A.; Ellis, D.E. The electronic properties of an oxygen vacancy at ZrO_2-terminated (001) surfaces of a cubic $PbZrO_3$: Computer simulations from first principles. *Phys. Chem. Chem. Phys.* **2008**, *10*, 4258–4263. [CrossRef]
108. Wang, G.Z.; Li, C.R.; Cui, J.; Man, Z.Y. Ab initio study of $ATiO_3$ (001) surfaces. *Surf. Interface Anal.* **2009**, *41*, 918–923. [CrossRef]
109. Eglitis, R.I.; Rohlfing, M. First-principles calculations of the atomic and electronic structure of $SrZrO_3$ and $PbZrO_3$ (001) and (011) surfaces. *J. Phys. Condens. Matter* **2010**, *22*, 415901.
110. Dionot, J.; Geneste, G.; Mathieu, C.; Barret, N. Surface polarization, rumpling, and domain ordering of strained ultrathin $BaTiO_3$ (001) films with in-plane and out-of-plane polarization. *Phys. Rev. B* **2014**, *90*, 014107. [CrossRef]
111. Shanavas, K.V. Theoretical study of the cubic Rashba effect at the $SrTiO_3$ (001) surfaces. *Phys. Rev. B* **2016**, *93*, 045108.
112. Slassi, A.; Hammi, M.; Rhazouani, O.E. Surface Relaxation, Surface Energies, and Electronic Structures of $BaSnO_3$ (001) surfaces: Ab initio Calculations. *J. Electron. Mater.* **2017**, *46*, 4133–4139.
113. Saghayezhian, M.; Sani, S.M.R.; Zhang, J.; Plummer, E.W. Rumpling and Enhanced Covalency at the $SrTiO_3$ (001) surface. *J. Phys. Chem. C* **2019**, *123*, 8086–8091.
114. Guedes, E.B.; Jensen, T.W.; Naamneh, M.; Chikina, A.; Dahm, R.T.; Yun, S.; Chiabrera, F.M.; Plumb, N.C.; Dil, J.H.; Shi, M.; et al. Disclosing the response of the surface electronic structure in $SrTiO_3$ (001) to strain. *J. Vac. Sci. Technol. A* **2022**, *40*, 013213.
115. Zhou, Z.; Zhan, C.; Kan, E. Understanding the piezocatalytic properties of the $BaTiO_3$ (001) surface via density functional theory. *Phys. Chem. Chem. Phys.* **2023**, *25*, 8631–8640. [CrossRef]
116. Azevedo, S.A.; Laranjeira, J.A.S.; Silva, J.F.; Longo, E.; Sambrano, J.R. Ag-doped $SrTiO_3$: Enhanced water splitting for hydrogen production. *Int. J. Hydrogen Energy* **2024**, *79*, 199–207. [CrossRef]
117. Schafranek, R.; Li, S.; Chen, F.; Wu, W.; Klein, A. $PbTiO_3/SrTiO_3$ interface: Energy band alignment and its relation to the limits of Fermi level variation. *Phys. Rev. B* **2011**, *84*, 045317.
118. Wu, P.; Ma, X.; Li, Y.; Gopalan, V.; Chen, L.Q. Dipole spring ferroelectrics in superlattice $SrTiO_3/BaTiO_3$ thin films exhibiting constricted hysteresis loops. *Appl. Phys. Lett.* **2012**, *100*, 092905.
119. Shah, S.H.; Bristowe, P.D.; Kolpak, A.M.; Rappe, A.M. First principles study of three-componet $SrTiO_3/BaTiO_3/PbTiO_3$ ferroelectric superlattices. *J. Mater. Sci.* **2008**, *43*, 3750–3760.
120. Gao, Y.C.; Duan, C.G.; Tang, X.D.; Hu, Z.G.; Yang, P.; Zhu, Z.; Chu, J. A first principles study of the intrinsic asymmetric ferroelectricity of the $SrTiO_3$-$BaTiO_3$-$CaTiO_3$ tricolor superlattice at the nanoscale. *J. Phys. Condens. Matter* **2013**, *25*, 165901.
121. Jiang, Z.; Xu, B.; Li, F.; Wang, D.; Jia, C.L. Electric dipole sheets in $BaTiO_3/BaZrO_3$ superlattices. *Phys. Rev. B* **2015**, *91*, 014105. [CrossRef]
122. Piskunov, S.; Eglitis, R.I. First principles hybrid DFT calculations of $BaTiO_3/SrTiO_3$ (001) interface. *Solid State Ion.* **2015**, *274*, 29–33.
123. Piskunov, S.; Eglitis, R.I. Comparative ab initio calculations of $SrTiO_3/BaTiO_3$ and $SrZrO_3/PbZrO_3$ (001) heterostructures. *Nucl. Instrum. Methods B* **2016**, *374*, 20–23. [CrossRef]

124. Eglitis, R.I.; Piskunov, S.; Zhukovskii, Y.F. Ab initio calculations of $PbTiO_3/SrTiO_3$ (001) heterostructures. *Phys. Status Solidi B* **2016**, *13*, 913–920. [CrossRef]
125. Eglitis, R.I.; Bocharov, D.; Piskunov, S.; Jia, R. Review of First Principles Simulations of STO/BTO, STO/PTO, and SZO/PZO (001) Heterostructures. *Crystals* **2023**, *13*, 799. [CrossRef]
126. Eglitis, R.I.; Piskunov, S.; Popov, A.I.; Purans, J.; Bocharov, D.; Jia, R. Systematic Trends in Hybrid-DFT Computations of $BaTiO_3/SrTiO_3$, $PbTiO_3/SrTiO_3$ and $PbZrO_3/SrZrO_3$ (001) Hetero Structures. *Condens. Matter* **2022**, *7*, 70. [CrossRef]
127. Shoron, O.F.; Raghavan, S.; Freeze, C.R.; Stemmer, S. $BaTiO_3/SrTiO_3$ heterostructures for ferroelectric field effect transistors. *Appl. Phys. Lett.* **2017**, *110*, 232902. [CrossRef]
128. Cao, Y.; Wang, Z.; Park, S.Y.; Yuan, Y.; Liu, X.; Nikitin, S.M.; Akamatsu, H.; Kareev, M.; Middey, S.; Meyers, D.; et al. Artificial two-dimensional polar metal at room temperature. *Nat. Commun.* **2018**, *9*, 1547. [CrossRef]
129. Bonini, J.; Bennett, J.W.; Chandra, P.; Rabe, K.M. First-principles bulk-layer model for dielectric and piezoelectric response in superlattices. *Phys. Rev. B* **2019**, *99*, 104107.
130. Jia, F.; Wu, S.; Zhao, G.; Liu, C.; Ren, W. Structural and electronic properties of two-dimensional freestanding $BaTiO_3/SrTiO_3$ heterostructures. *Phys. Rev. B* **2020**, *101*, 144106. [CrossRef]
131. Piyanzina, I.I.; Pavlov, D.P.; Jagličič, Z.; Shulyaev, D.A.; Tayurski, D.A.; Kabanov, V.V.; Mamin, R.F. Structural and magnetic properties of ferroelectric/dielectric $BaTiO_3/LaMnO_3$ and $BaTiO_3/SrTiO_3$ heterostructures. *Ferroelectrics* **2021**, *575*, 144–150.
132. Chen, B.; Gauquelin, N.; Strkal, N.; Huang, S.; Halisdemis, U.; Nguyen, M.D.; Jannis, D.; Sarott, M.F.; Eltes, F.; Abel, S.; et al. Signatures of enhanced out-of-plane polarization in asymmetric $BaTiO_3$ superlattices integrated on silicon. *Nat. Commun.* **2022**, *13*, 265. [CrossRef] [PubMed]
133. Yang, F.; Liang, Y.; Wu, P. Vortex structure in relaxed $BaTiO_3/SrTiO_3$ superlattice. *Appl. Phys. Express* **2023**, *16*, 055002. [CrossRef]
134. Gómez-Ortiz, F.; Graf, M.; Junquera, J.; Íñiguez-González, J.; Aramberi, H. Liquid-Crystal-Like Dynamic Transition in Ferroelectric-Dielectric Superlattices. *Phys. Rev. Lett.* **2024**, *133*, 066801.
135. Eglitis, R.I.; Christensen, N.E.; Kotomin, E.A.; Postnikov, A.V.; Borstel, G. First-principles and semiempirical calculations for F center in $KNbO_3$. *Phys. Rev. B* **1997**, *56*, 8599–8604.
136. Park, C.H.; Chadi, D.J. Microscopic study of oxygen-vacancy defects in ferroelectric perovskites. *Phys. Rev. B* **1998**, *57*, R13961–R13964. [CrossRef]
137. Zhang, W.F.; Yin, Z.; Zhang, M.S.; Du, Z.L.; Chen, W.C. Roles of defects and grain sizes in photoluminescence of nanocrystalline $SrTiO_3$. *J. Phys. Condens. Matter* **1999**, *11*, 5655.
138. Donnerberg, H.; Birkholz, A. Ab initio study of oxygen vacancies in $BaTiO_3$. *J. Phys. Condens. Matter* **2000**, *12*, 8239. [CrossRef]
139. Astala, R.; Bristowe, P.D. Ab initio and classical simulations of defects in $SrTiO_3$. *Comput. Mater. Sci.* **2001**, *22*, 81–86. [CrossRef]
140. Stashans, A.; Serrano, S. A quantum-chemical study of polar $SrTiO_3$ (110) surface and oxygen-vacancy defects therein. *Surf. Sci.* **2002**, *497*, 285–293. [CrossRef]
141. Muller, D.A.; Nakagawa, N.; Ohtomo, A.; Grazu, J.L.; Hwang, H.Y. Atomic-scale imaging of nanoengineered oxygen vacancy profiles in $SrTiO_3$. *Nature* **2004**, *430*, 657–661. [CrossRef]
142. Carrasco, J.; Illas, F.; Lopez, N.; Kotomin, E.A.; Zhukovskii, Y.F.; Evarestov, R.A.; Mastrikov, Y.A.; Piskunov, S.; Maier, J. First-principles calculations of the atomic and electronic structure of F centers in the bulk and on the (001) surface of $SrTiO_3$. *Phys. Rev. B* **2006**, *73*, 064106. [CrossRef]
143. Lee, H.S.; Mizoguchi, T.; Yamamoto, T.; Kang, S.J.L.; Ikuhara, Y. First-principles calculation of defect energetics in cubic-$BaTiO_3$ and a comparison with $SrTiO_3$. *Acta Mater.* **2007**, *55*, 6535–6540. [CrossRef]
144. Alexandrov, V.E.; Kotomin, E.A.; Maier, J.; Evarestov, R.A. First-principles study of bulk and surface oxygen vacancies in $SrTiO_3$ crystal. *Solid State Mater.* **2009**, *72*, 53–57. [CrossRef]
145. Choi, M.; Oba, F.; Tanaka, I. Electronic and structural properties of the oxygen vacancy in $BaTiO_3$. *Appl. Phys. Lett.* **2011**, *98*, 172901. [CrossRef]
146. El-Mellouhi, F.; Brother, E.N.; Lucero, M.J.; Scuseria, G.E. Neutral defects in $SrTiO_3$ studied with screened hybrid density functional theory. *J. Phys. Condens. Matter* **2013**, *25*, 135501. [CrossRef]
147. Chen, C.F.; King, G.; Dicker, R.M.; Papin, P.A.; Gupta, S.; Kellog, W.R.; Wu, G. Oxygen-deficient $BaTiO_{3-x}$ perovskite as an efficient bifunctional oxygen electrocatalyst. *Nano Energy* **2015**, *13*, 423–432. [CrossRef]
148. Clabel, J.L.; Rivera, V.A.G.; Nogueira, I.C.; Leite, E.R.; Pereira-da-Silva, M.A.; Siu, M.; Marega, E. Effects of defects grain size, and thickness on the optical properties of $BaTiO_3$ thin films. *J. Lumin.* **2017**, *192*, 969–974. [CrossRef]
149. Al-Zubi, A.; Bihlmayer, G.; Blügel, S. Electronic Structure of Oxygen-Deficient $SrTiO_3$ and $Sr2TiO_4$. *Crystals* **2019**, *9*, 580. [CrossRef]
150. Rusevich, L.L.; Tyunina, M.; Kotomin, E.A.; Nepomniashchaia, N.; Dejneka, A. The electronic properties of $SrTiO_{3-\delta}$ with oxygen vacancies or substitutions. *Sci. Rep.* **2021**, *11*, 23341. [CrossRef]
151. Yang, Y.; Fang, W.; Mi, Y.; Yan, J.; Li, X.; Shangguan, W. Enhanced photocatalytic overall water splitting by tuning the relative concentration ratio of bulk defects to surface defects in $SrTiO_3$. *Int. J. Hydrogen Energy* **2023**, *48*, 1360–1369. [CrossRef]

152. Wang, Z.; Meng, X.; Guo, Q.; Su, C.; Deng, G.; Liu, H.; Yao, Z.; Zhang, S.; Liu, H.; Hao, H. Formation and evolution of oxygen vacancy layer in $BaTiO_3$ dielectric ceramics under thermal and electric field stimuli. *Acta Mater.* **2025**, *299*, 121450. [CrossRef]
153. Dovesi, R.; Saunders, V.R.; Roetti, C.; Orlando, R.; Zicovich-Wilson, C.M.; Pascale, F.; Civalleri, B.; Doll, K.; Harrison, N.M.; Bush, I.J.; et al. *CRYSTAL-2017 User Manual*; University of Torino: Turin, Italy, 2017.
154. Lee, C.; Yang, W.; Parr, R.G. Development of the Colle-Salvetti correlation-energy formula into a functional of the electron density. *Phys. Rev. B* **1988**, *37*, 785–789. [CrossRef] [PubMed]
155. Perdew, J.P.; Wang, Y. Accurate and simple density functional for the electronic exchange energy: Generalized gradient approximation. *Phys. Rev. B* **1986**, *33*, 8800–8802. Erratum in *Phys. Rev. B* **1989**, *40*, 3399. https://doi.org/10.1103/PhysRevB.40.3399. [CrossRef]
156. Perdew, J.P.; Wang, Y. Accurate and simple analytic representation of the electron-gas correlation energy. *Phys. Rev. B* **1992**, *45*, 13244–13249. [CrossRef]
157. Dovesi, R.; Orlando, R.; Roetti, C.; Pisani, C.; Saunders, V.R. The Periodic Hartree-Fock Method and Its Implementation in the Crystal Code. *Phys. Status Solidi B* **2000**, *217*, 63–88. [CrossRef]
158. Ziesche, P.; Kurth, S.; Perdew, J.P. Density functionals from LDA to GGA. *Comput. Mater. Sci.* **1998**, *11*, 122–127. [CrossRef]
159. Shi, H.; Chang, L.; Jia, R.; Eglitis, R.I. Ab initio calculations of the Transfer and Aggregation of F centers in CaF_2. *J. Phys. Chem. C* **2012**, *116*, 4832–4839. [CrossRef]
160. Shi, H.; Eglitis, R.I.; Borstel, G. Ab initio calculations of the CaF_2 electronic structure and *F* centers. *Phys. Rev. B* **2005**, *72*, 045109. [CrossRef]
161. Hohenberg, P.; Kohn, W. Inhomogeneous Electron Gas. *Phys. Rev.* **1964**, *136*, B864–B871. [CrossRef]
162. Kohn, W.; Sham, L.J. Self-Consistent Equations Including Exchange and Correlation Effects. *Phys. Rev.* **1965**, *140*, A1133–A1138. [CrossRef]
163. Monkhorst, H.J. Special points for Brillouin-zone integrations. *Phys. Rev. B* **1976**, *13*, 5188. [CrossRef]
164. Mulliken, R.S. Electronic Population Analysis on LCAO-MO Molecular Wave Functions. *J. Chem. Phys.* **1955**, *23*, 1833–1840. [CrossRef]
165. Eglitis, R.I.; Kotomin, E.A.; Trepakov, V.A.; Kapphan, S.E.; Borstel, G. Quantum chemical modelling of electron polarons and green luminescence in $PbTiO_3$ perovskite crystals. *J. Phys. Condens. Matter* **2002**, *14*, L647. [CrossRef]
166. Piskunov, S.; Heifets, E.; Eglitis, R.I.; Borstel, G. Bulk properties and electronic structure of $SrTiO_3$, $BaTiO_3$, $PbTiO_3$ perovskites: An ab initio HF/DFT study. *Comput. Mater. Sci.* **2004**, *29*, 165–178. [CrossRef]
167. Tasker, P.W. The stability of ionic crystal surfaces. *J. Phys. C Solid State Phys.* **1979**, *12*, 4977. [CrossRef]
168. Schlegel, H.B. Optimization of equilibrium geometries and transition structures. *J. Comput. Chem.* **1982**, *3*, 214–218. [CrossRef]
169. Civalleri, B.; D'Arco, P.; Orlando, R.; Saunders, V.R.; Dovesi, R. Hartree-Fock geometry optimization of periodic systems with the CRYSTAL code. *Chem. Phys. Lett.* **2001**, *348*, 131–138. [CrossRef]
170. Eglitis, R.I.; Piskunov, S. First principles calculations of $SrZrO_3$ bulk and ZrO_2-terminated (001) surface *F* centers. *Comput. Condens. Matter* **2016**, *7*, 1–6. [CrossRef]
171. Eglitis, R.I. Theoretical Modelling of the Energy Surface (001) and Topology of $CaZrO_3$ Perovskite. *Ferroelectrics* **2015**, *483*, 75–85.
172. Hellwege, K.H.; Helwege, A.M. Ferroelectrics and Related Substances. In *Landolt-Bornstein, New Series, Group III*; Springer: Berlin/Heidelberg, Germany, 1969; Volume 3.
173. Mabud, S.A.; Glazer, A.M. Lattice parameters and birefringence in $PbTiO_3$ single crystals. *J. Appl. Crystallogr.* **1979**, *12*, 49–53. [CrossRef]
174. Ali, R.; Yashima, M. Space group and crystal structure of the Perovskite $CaTiO_3$ from 296 to 1720 K. *J. Solid State Chem.* **2005**, *178*, 2867–2872.
175. Kennedy, B.J.; Howard, C.J.; Chakoumakos, B.C. High-temperature phase transitions in $SrZrO_3$. *Phys. Rev. B* **1999**, *59*, 4023–4027. [CrossRef]
176. Matthews, M.D.; Mirza, E.B.; Momin, A.C. High-temperature X-ray diffractiometric studies of $CaZrO_3$, $SrZrO_3$ and $BaZrO_3$. *J. Mater. Sci. Lett.* **1991**, *10*, 305–306. [CrossRef]
177. Aoyagi, S.; Kuroiwa, Y.; Sawada, A.; Tanaka, H.; Nishibori, E.; Takata, M.; Sakata, M. Direct Observation of Cavalency between O and Disordered Pb in Cubic $PbZrO_3$. *J. Phys. Soc. Jpn.* **2002**, *71*, 2353–2356.
178. Benthem, K.; Elsässer, C.; French, R.H. Bulk electronic structure of $SrTiO_3$: Experiment and theory. *J. Appl. Phys.* **2001**, *90*, 6156–6164. [CrossRef]
179. Eglitis, R.I. Ab initio calculations of the atomic and electronic structure of $BaZrO_3$ (111) surfaces. *Solid State Ion.* **2013**, *230*, 43–47.
180. Robertson, J. Band offsets of wide-band-gap oxides and implications for future electronic devices. *J. Vacuum. Sci. Technol.* **2000**, *18*, 1785–1791. [CrossRef]
181. Eglitis, R.I.; Purans, J.; Popov, A.I.; Jia, R. Tendencies in ABO_3 perovskite and SrF_2, BaF_2 and CaF_2 bulk and surface *F*-center ab initio computations at high symmetry cubic structure. *Symmetry* **2021**, *13*, 1920. [CrossRef]

182. Sokolov, M.; Eglitis, R.I.; Piskunov, S.; Zhukovskii, Y.F. Ab initio hybrid DFT calculations of $BaTiO_3$ bulk and BaO-terminated (001) surface *F*-centers. *Int. J. Mod. Phys. B* **2017**, *31*, 1750251.
183. Eglitis, R.; Popov, A.I.; Purans, J.; Jia, R. First principles hybrid Hartree-Fock-DFT calculations of bulk and (001) surface *F* centers in oxide perovskites and alkali-earth fluorides. *Low Temp. Phys.* **2020**, *46*, 1206–1212.
184. Eglitis, R.I.; Kotomin, E.A.; Popov, A.I.; Kruchinin, S.P.; Jia, R. Comparative ab initio calculations of $SrTiO_3$, $BaTiO_3$, $PbTiO_3$ and $SrZrO_3$ (001) and (111) surfaces as well as oxygen vacancies. *Low Temp. Phys.* **2022**, *48*, 80–88.
185. Eglitis, R.I.; Purans, J.; Popov, A.I.; Piskunov, S.; Jia, R.; Kruchinin, S.P. ABO_3 perovskite as well as BaF_2, SrF_2 and CaF_2 bulk and surface *F*-center first principles predictions. *Mod. Phys. Lett. B* **2024**, *38*, 2342004. [CrossRef]
186. Padilla, J.; Vanderbilt, D. Ab initio study of $SrTiO_3$ surfaces. *Surf. Sci.* **1998**, *418*, 64–70.
187. Bickel, N.; Schmidt, G.; Heinz, K.; Müller, K. Ferroelectric relaxation of the $SrTiO_3$ (100) surface. *Phys. Rev. Lett.* **1989**, *62*, 2009–2011. [CrossRef] [PubMed]
188. Hikita, T.; Hanada, T.; Kudo, M.; Kawai, M. Structure and electronic state of the TiO_2 and SrO terminated $SrTiO_3$ (100) surfaces. *Surf. Sci.* **1993**, *287–288*, 377–381. [CrossRef]